DOI:
10.1002/mrm.27521

Document Version
Peer reviewed version

Multi-modal synergistic PET and MR reconstruction using mutually weighted quadratic priors

Journal:	*Magnetic Resonance in Medicine*
Manuscript ID	MRM-18-19027.R3
Wiley - Manuscript type:	Full Paper
Date Submitted by the Author:	15-Aug-2018
Complete List of Authors:	MEHRANIAN, ABOLFAZL; King's College London, Department of Biomedical Engineering Belzunce, Martin; King's College London, Department of Biomedical Engineering McGinnity, Colm; King's College London, King's College London & Guy's and St Thomas' PET Centre Bustin, Aurélien; King's College London, Department of Biomedical Engineering Prieto, Claudia; King's College London, Department of Biomedical Engineering Hammers, Alexander; King's College London, King's College London & Guy's and St Thomas' PET Centre Reader, Andrew; King's College London, Department of Biomedical Engineering
Research Type:	Parallel imaging < Technique Development < Technical Research, Compressed sensing < Reconstruction < Technique Development < Technical Research
Research Focus:	Brain < Neurological

Multi-modal synergistic PET and MR reconstruction using mutually weighted quadratic priors

Abolfazl Mehranian[1], Martin A. Belzunce[1], Colm J. McGinnity[2], Aurelien Bustin[1], Claudia Prieto[1], Alexander Hammers[2] and Andrew J. Reader[1]

School of Biomedical Engineering and Imaging Sciences, King's College London, [1]Department of Biomedical Engineering and [2]King's College London & Guy's and St Thomas' PET Centre, St. Thomas' Hospital, London, UK

Corresponding author:

Abolfazl Mehranian, PhD.

Research Associate
School of Biomedical Engineering and Imaging Sciences
King's College London
3rd Floor, Lambeth Wing
St Thomas' Hospital
London, SE1 7EH
Abolfazl.Mehranian@kcl.ac.uk

Running Head

Multi-modal PET-MR reconstruction

Word count: ~5600

Number of tables and figures: 10

ABSTRACT

Purpose:

To propose a framework for synergistic reconstruction of PET-MR and multi-contrast MR data in order to improve the image quality obtained from noisy PET data and from undersampled MR data.

Theory and Methods:

Weighted quadratic priors were devised to preserve common boundaries between PET-MR images while reducing noise, PET Gibbs ringing and MR undersampling artefacts. These priors are iteratively reweighted using normalized multi-modal Gaussian similarity kernels. Synergistic PET-MR reconstructions were built upon the PET maximum *a posteriori* expectation maximization algorithm and the MR regularized sensitivity encoding method. The proposed approach was compared to conventional methods, total variation (TV) and prior-image weighted quadratic (wQ) regularization methods. Comparisons were performed on a simulated FDG-PET and T1/T2-weighted MR brain phantom, two in-vivo T1/T2-weighted MR brain datasets, and an in-vivo FDG-PET and FLAIR/T1-weighted MR brain dataset.

Results:

Simulations showed that synergistic reconstructions achieve the lowest quantification errors for all image modalities compared to conventional, TV and wQ methods. While TV regularization preserved modality-unique features, this method failed to recover PET details nor was able to reduce MR artefacts compared to our proposed method. For in-vivo MR data, our method maintained similar image quality for 3x and 14x accelerated data. Reconstruction of the PET-MR dataset also demonstrated improved performance of our method compared to the conventional independent methods, in terms of reduced Gibbs and undersampling artefacts.

Conclusion:

The proposed methodology offers a robust multi-modal synergistic image reconstruction framework which can be readily built upon existing established algorithms.

1. INTRODUCTION

Simultaneous positron emission tomography (PET) and magnetic resonance imaging (MRI) systems have opened the way for synergistic reconstruction of PET-MR data to improve image quality (1–3), particularly for low-count PET data and/or highly undersampled MRI data.

It is known that PET reconstruction using the conventional maximum-likelihood expectation maximization (MLEM) algorithm exhibits noise and loss of details, due to noise in the data and the limited detector resolution. Hence, co-registered high-resolution MR images have been used to guide the reconstruction of PET data using maximum *a posteriori* (MAP) expectation maximization (MAPEM) algorithms. Quadratic (Tikhonov) and total variation (TV) priors are among the most commonly used MAP priors (4,5). However, mismatches between PET and MR images may introduce false features or suppress true ones in the reconstructed images. Nonetheless, the complementary information of multi-contrast MR images available in simultaneous PET-MR scanners can be employed to cope with these mismatches (6).

On the other hand, MR imaging often requires long acquisitions, particularly for multi-parametric imaging. Conventional fast acquisitions include partial Fourier (7) and parallel MRI, such as sensitivity encoding (SENSE) (8), where the acquisition is accelerated by undersampling the k-space data. At high acceleration factors, the conventional reconstructions show extensive noise amplification and/or aliasing artefacts. Hence, similar to PET, different regularization methods have been investigated for incorporation of prior knowledge into MR image reconstruction (9,10) among which compressed sensing (CS) and sparsity regularization are the most successful ones (11–13). In multi-contrast and longitudinal MR scans, existing MR images of the same or different contrasts can be also used to form additional prior knowledge about the MR image being reconstructed (14–19). Similar to MR-guided PET reconstruction, prior image guided MR reconstruction is also subject to the mismatches between MR images, hence the joint or synergistic reconstruction of multi-contrast undersampled MR images have been explored (20–22). Bilgic *et al* (23) proposed reconstruction of MR images using joint image gradients of multi-contrast images. Weizman *et al* (21) studied separate TV priors defined on each MR image contrast and an additional reweighted L_1 norm prior defined on the difference of the MR images.

Synergistic PET and MR image reconstruction has also been recently explored to exploit the complementary information of the PET-MR images. The benefits of such reconstructions are challenged by the need for the development of i) a model-based joint prior that favours common features between PET and multi-contrast MR images, irrespective of their relative signal intensities and their relative contrast orientations while preserving modality unique features. ii) a robust and stable optimization algorithm with preferably few hyperparameters. Ehrhardt *et al* (1) reported the first attempt in synergistic PET-MR image reconstruction based on the parallelism of PET-MR level sets (PLS), while Knoll *et al* (2) proposed a total generalized variation (TGV) regularization based on the nuclear norm. Despite promising results, their methods depend on relative signal intensities. In (3), we recently proposed a generalized TV prior with an alternating scaling scheme to handle the relative signal intensity issue. Simulation results showed that our algorithm can outperform the PLS and joint TV priors, however, the proposed scaling scheme was designed to match the magnitude of PET and MR image gradients using a single global scale factor. Hence, this algorithm is not efficient and robust for all regions in PET-MR images with different gradient magnitudes. In addition, similar to previous work, a relatively complex optimization algorithm was chosen.

In this study, we propose a framework for synergistic PET and multi-contrast MR image reconstruction. In this framework, the PET and MR images are reconstructed using well-established EM and iterative SENSE reconstruction algorithms and are regularized using adaptively weighted multi-modal quadratic priors. These priors i) are able to preserve modality unique features through calculating weighting factors from all image modalities, ii) are independent of the *relative* signal intensities and contrast orientations of MR or PET-MR images and iii) easily accommodate synergistic reconstruction of multiple PET or MR datasets. Synergistic reconstruction of multiple datasets has also been recently reported in (24). The proposed prior is similar to the Bowsher prior, however with the difference that similarity coefficients are progressively derived from all multi-modal images rather than being precalculated as in the Bowsher prior (6). In this study, we present our results using realistic 3D simulations, in-vivo undersampled 3D MR data and an in-vivo PET-MR dataset for the different guided and synergistic reconstruction methods.

2. THEORY

Synergistic reconstruction of PET and MR data

The synergistic reconstruction of the PET image, $\boldsymbol{u} \in \mathbb{R}^{N_u}$, and MR images, $\boldsymbol{v}^{(k)} \in \mathbb{C}^{N_k}$, $k = 1, \dots, V$, of different contrasts can be achieved by the following optimization (3):

$$\begin{aligned}\left(\hat{\boldsymbol{u}}, \hat{\boldsymbol{v}}^{(1)}, \dots, \hat{\boldsymbol{v}}^{(V)}\right) \\ = \underset{\boldsymbol{u}, \boldsymbol{v}^{(1)}, \dots, \boldsymbol{v}^{(V)}}{\operatorname{argmax}} \left\{ \left(\sum_{i=1}^{M_u} \left(y_i \log\left([\boldsymbol{P}\boldsymbol{u}]_i + \bar{r}_i\right) - [\boldsymbol{P}\boldsymbol{u}]_i - \bar{r}_i \right) \right) \right. \\ \left. - \left(\frac{1}{2} \sum_{k=1}^{V} \sum_{l=1}^{L} \sum_{i=1}^{M_k} w_{li}^{(k)} \left| \left[\boldsymbol{E}^{(k)} \boldsymbol{v}^{(k)}\right]_{li} - s_{li}^{(k)} \right|^2 \right) - R\left(\boldsymbol{u}, \boldsymbol{v}^{(1)}, \dots, \boldsymbol{v}^{(V)}\right) \right\}\end{aligned} \quad [1]$$

where the three terms of the objective function correspond to the PET data fidelity, MR data fidelity and the joint modality prior. $\boldsymbol{y} \in \mathbb{Z}^{M_u}$ is the PET sinogram data, $\boldsymbol{P} \in \mathbb{R}^{M_u \times N_u}$ is the PET system matrix (composed of the geometric transition matrix, the scanner's point spread function (PSF), attenuation and normalization factors), $\bar{\boldsymbol{r}} \in \mathbb{R}^{M_u}$ is an estimate of the mean PET background coincidences (randoms and scatters), N_u and M_u are the number of image voxels and sinogram bins. $\boldsymbol{s}^{(k)} \in \mathbb{C}^{M_k L}$ is the k-space data for the kth MR image contrast, $\boldsymbol{E}^{(k)} \in \mathbb{C}^{M_k L \times N_k}$ is its corresponding MR encoding matrix (composed of a discrete Fourier transform, k-space undersampling matrix and coil sensitivity profiles). M_k, L and N_k are the number of k-space samples, coils and voxels for the kth image contrast, respectively. $w_{li}^{(k)}$ is an element of a $\boldsymbol{W}^{(k)} \in \mathbb{R}^{M_k L \times M_k L}$ weighting matrix obtained from the inversion of the noise covariance matrix (25). In this study, the joint prior R was defined as the sum of mutually weighted quadratic priors as follows:

$$R\left(\boldsymbol{u}, \boldsymbol{v}^{(1)}, \dots, \boldsymbol{v}^{(V)}\right) = \frac{1}{2} \sum_{j=1}^{N_u} \sum_{b \in \mathcal{N}_j} \beta_u \xi_{jb}^{u} \omega_{jb}^{u} \left(u_j - u_b\right)^2 + \frac{1}{2} \sum_{k=1}^{V} \sum_{j=1}^{N_k} \sum_{b \in \mathcal{N}_j} \beta_{v^{(k)}} \xi_{jb}^{v^{(k)}} \omega_{jb}^{v^{(k)}} \left(v_j^{(k)} - v_b^{(k)}\right)^2 \quad [2]$$

where β is a regularization parameter and ξ_{jb} and ω_{jb} are coefficients used to modulate the intensity differences between voxel j and b based on their Euclidean proximity and intensity similarity in a neighbourhood $\mathcal{N}_j$, respectively. The proximity coefficients were defined as:

$$\xi_{jb} = \frac{1}{\sqrt{\sum_{i=1}^{3}(j^{(i)} - b^{(i)})^2}} \quad [3]$$

where $\{j^{(i)}\}$ and $\{b^{(i)}\}$ are the Cartesian coordinates of the jth and bth voxel. In the proposed prior, the similarity coefficients are alternatingly calculated from both PET-MR images using the following joint coefficients (6):

$$\omega_{jb} = \frac{\mathcal{G}(\hat{u}_j, \hat{u}_b, \sigma_u)\mathcal{G}(\hat{v}_j^{(1)}, \hat{v}_b^{(1)}, \sigma_1) \dots \mathcal{G}(\hat{v}_j^{(V)}, \hat{v}_b^{(V)}, \sigma_{v^{(V)}})}{\sum_{j=1}^{N}\mathcal{G}(\hat{u}_j, \hat{u}_b, \sigma_u)\mathcal{G}\left(\hat{v}_j^{(1)}, \hat{v}_b^{(1)}, \sigma_{v^{(1)}}\right) \dots \mathcal{G}\left(\hat{v}_j^{(V)}, \hat{v}_b^{(V)}, \sigma_{v^{(V)}}\right)} \quad [4]$$

$$\mathcal{G}(q, r, \sigma) = \frac{1}{\sqrt{2\pi}\sigma}\exp\left(-\frac{(q-r)^2}{2\sigma^2}\right)$$

where $\hat{\boldsymbol{u}}$ and $\hat{\boldsymbol{v}}^{(k)}$ are the current estimates of the PET and MR images, obtained iteratively in the case of synergistic reconstruction or are prior images in the case of guided PET or MR reconstruction. These coefficients are composed of the product of Gaussian similarity kernels calculated between voxel j and b in a neighbourhood $\mathcal{N}_j$ for each image modality. The role of ω_{jb} is to assign a lower penalty on the local differences that are associated with a boundary identified uniquely from the PET image or MR image or mutually from all PET and MR images. In PET unique boundaries, the MR-derived Gaussian kernels in ω_{jb} are uniform, whereas in shared boundaries they have the same structural similarity, irrespective of contrast orientation and relative signal intensity. Therefore, the product of the kernels will preserve the modality unique boundaries and encourage the formation of shared ones.

Since PET and MR images may all have different matrix and voxel sizes, the ω_{jb} coefficients in Eq. [4] must be uniquely calculated for each modality. Hence, registration and resampling operators, $\boldsymbol{\Phi}_{\boldsymbol{x}\to\boldsymbol{y}}$, need to be defined to spatially map image modality, $\boldsymbol{x}$, to a given image, $\boldsymbol{y}$ (see step 3 in *Proposed Algorithm* for more details). In this study, we followed an alternating optimization of Eq. [1]. As summarized in *Proposed Algorithm,* the optimization consists of three main steps: i) MAPEM image reconstruction of PET data using a weighted quadratic prior, employing De Pierro's decoupling rule for regularization (26,27) with P_{iter} iterations, ii) SENSE MR image reconstruction using a weighted quadratic prior and the conjugate gradient (CG) algorithm (28) with M_{iter} iterations and iii) calculation of the similarity coefficients used during PET and MR reconstruction.

In this algorithm, $\boldsymbol{q}$ is PET sensitivity image, $\boldsymbol{D}$ is a derivative matrix for calculation of local differences between image voxels, $\boldsymbol{\xi}$ and $\boldsymbol{\omega}$ are diagonal weighting matrices with diagonal elements calculated by Eq. [3-4], respectively. In this study, the proposed synergistic algorithm was employed for different synergistic PET-MR and MR reconstructions in comparison with a number of separate reconstruction methods as summarized in Supporting Information Table S1.

Proposed Algorithm: Synergistic reconstruction of PET and MR data

Initialize PET parameters: $\boldsymbol{u}^0 = \mathbf{1}$, $\boldsymbol{\omega}^u = \mathbf{1}$, σ_u, β_u

Initialize MR parameters: $\boldsymbol{v}^{(0,k)} = \mathbf{0}$, $\boldsymbol{\omega}^{(k)} = \mathbf{1}$, σ_k, β_k for $k = 1, \dots, V$

While *A stopping criterion is met*

1. MAP PET reconstruction using De Pierro's method.

For $n = 0, \dots, P_{iter}$

1.a. Expectation maximization (EM) update:

$$\boldsymbol{u}_{EM}^{n+1} = \frac{\boldsymbol{u}^n}{\boldsymbol{P}^T\mathbf{1}}\boldsymbol{P}^T\left(\frac{\boldsymbol{y}}{\boldsymbol{P}\boldsymbol{u}^n + \bar{\boldsymbol{r}}_i}\right) \quad [5]$$

1.b. Regularization:

$$u_j^{n+1} = \frac{2q_j u_{EM,j}^{n+1}}{B + \sqrt{B^2 + 4\beta_u q_j u_{EM,j}^{n+1}\sum_{b\in\mathcal{N}_j}\xi_{jb}^u\omega_{jb}^u}}$$
$$B = q_j - \frac{\beta_u}{2}\sum_{b\in\mathcal{N}_j}\xi_{jb}^u\omega_{jb}^u\left(u_j^n + u_b^n\right), \qquad q_j = \sum_i p_{ij} \quad [6]$$

End

2. MR SENSE reconstruction through solving $\boldsymbol{x} = \boldsymbol{A}\boldsymbol{b}$, using the CG algorithm:

where $\boldsymbol{x} = \boldsymbol{v}^{(n+1,k)}$, $\boldsymbol{A} = \left(\boldsymbol{E}^{(k)}\right)^H\boldsymbol{W}^{(k)}\boldsymbol{E}^{(k)} + \beta_k\left(\boldsymbol{D}^{(k)}\right)^T\boldsymbol{\xi}^{(k)}\boldsymbol{\omega}^{(k)}\boldsymbol{D}^{(k)}$ and $\boldsymbol{b} = \left(\boldsymbol{E}^{(k)}\right)^H\boldsymbol{W}^{(k)}\boldsymbol{s}^{(k)}$.

Initialize: $\boldsymbol{x}^0 = \boldsymbol{v}^{(n,k)}$, $\boldsymbol{r}^0 = \boldsymbol{b} - \boldsymbol{A}\boldsymbol{x}^0$, $\boldsymbol{p}^0 = \boldsymbol{r}^0$.

For $n = 0, \dots, M_{iter}$

2a. Calculate step size: $\alpha^i = \frac{(\boldsymbol{r}^i)^T\boldsymbol{r}^i}{(\boldsymbol{p}^i)^T\boldsymbol{A}\boldsymbol{p}^i}$

2b. Update the estimate $\boldsymbol{x}$: $\boldsymbol{x}^{i+1} = \boldsymbol{x}^i + \alpha^i\boldsymbol{p}^i$

2c. Update the residual: $\boldsymbol{r}^{i+1} = \boldsymbol{r}^i - \alpha^i\boldsymbol{A}\boldsymbol{p}^i$ [7]

2d. Update search direction: $\boldsymbol{p}^{i+1} = \boldsymbol{r}^{i+1} + \frac{(\boldsymbol{r}^{i+1})^T\boldsymbol{r}^{i+1}}{(\boldsymbol{r}^i)^T\boldsymbol{r}^i}\boldsymbol{p}^i$

End

$\boldsymbol{v}^{(n+1,k)} \leftarrow \boldsymbol{x}^{i+1}$.

3. Update the joint similarity coefficients:

3a. For $k = 1, \dots, V$, map the current MR image estimates into PET space, $\hat{\boldsymbol{v}}^{(k)} = \boldsymbol{\Phi}_{k\to u}\boldsymbol{v}^{(n+1,k)}$ and calculate PET similarity coefficients:

$$\omega_{jb}^u = \frac{\mathcal{G}\left(u_j^{n+1}, u_b^{n+1}, \sigma_u\right)\mathcal{G}\left(\hat{v}_j^{(1)}, \hat{v}_b^{(1)}, \sigma_{v^{(1)}}\right)\dots\mathcal{G}\left(\hat{v}_j^{(V)}, \hat{v}_b^{(V)}, \sigma_{v^{(V)}}\right)}{\sum_{j=1}^{N_u}\mathcal{G}\left(u_j^{n+1}, u_b^{n+1}, \sigma_u\right)\mathcal{G}\left(\hat{v}_j^{(1)}, \hat{v}_b^{(1)}, \sigma_{v^{(1)}}\right)\dots\mathcal{G}\left(\hat{v}_j^{(V)}, \hat{v}_b^{(V)}, \sigma_{v^{(V)}}\right)} \quad [8]$$

3b. For a given MR image contrast k', map the current PET and other MR image estimates, $k \neq k'$, to the k'th MR image space, $\hat{\boldsymbol{u}} = \boldsymbol{\Phi}_{u\to k'}\boldsymbol{u}^{n+1}$, $\hat{\boldsymbol{v}}^{(k)} = \boldsymbol{\Phi}_{k\to k'}\boldsymbol{v}^{(n+1,k)}$ and calculate k'th MR similarity coefficients:

$$\omega_{jb}^{k'} = \frac{\mathcal{G}\left(\hat{u}_j, \hat{u}_b, \sigma_u\right)\mathcal{G}\left(\hat{v}_j^{(1)}, \hat{v}_b^{(1)}, \sigma_{v^{(1)}}\right)\dots\mathcal{G}\left(v_j^{(n+1,k')}, v_b^{(n+1,k')}, \sigma_{v^{(k')}}\right)\dots\mathcal{G}\left(\hat{v}_j^{(V)}, \hat{v}_b^{(V)}, \sigma_{v^{(V)}}\right)}{\sum_{j=1}^{N_{k'}}\mathcal{G}\left(\hat{u}_j, \hat{u}_b, \sigma_u\right)\mathcal{G}\left(\hat{v}_j^{(1)}, \hat{v}_b^{(1)}, \sigma_{v^{(1)}}\right)\dots\mathcal{G}\left(v_j^{(n+1,k')}, v_b^{(n+1,k')}, \sigma_{v^{(k')}}\right)\dots\mathcal{G}\left(\hat{v}_j^{(V)}, \hat{v}_b^{(V)}, \sigma_{v^{(V)}}\right)} \quad [9]$$

End

3. METHODS

3.1. Simulated and real datasets

PET-MR Simulation. The BrainWeb phantom (29) was used to simulate an activity distribution of [^{18}F]fluorodeoxyglucose (FDG) in the brain, along with T1- and T2-weighted MR images. The matrix and voxel sizes of the PET phantom were set to 344×344×127 and 2.086×2.086×2.03 mm^3, while those of the MR phantoms were set to 230×230×254 and 1.043×1.043×1.015 mm^3. For the PET image, a grey-to-white matter activity ratio of 4:1 was considered while the MR intensity ratios were obtained from the BrainWeb simulator. Unique lesions were introduced in the PET and T1-weighted MR images with a volume of 0.76 mL (5.6 mm diameter) and 0.87 mL (7.6 mm diameter), respectively (see Figures 1-2 in the *Results* section for the location of the lesions). For the FDG-PET and T1-MR images, the lesion to white matter activity/intensity ratios were set to

6:1 and 2:1, respectively. PET simulations were performed for the Siemens Biograph mMR scanner including attenuation, normalization factors, 10% randoms and 30% scatter coincidences. Poisson noise realizations with a total of 90 million counts were generated for the PET phantom. Resolution degradation was modelled in image space with a 4.5 mm Gaussian kernel (30). MR simulations were performed for an MR scanner with a 5-channel coil, 100 mm coil radius and 150 mm coil distance from centre. Coil sensitivity maps were simulated based on Biot–Savart's law (31). For undersampled MR reconstructions, the k-spaces of the T1 and T2 images were contaminated with Gaussian noise and undersampled using Cartesian (undersampling factor of 6) and radial trajectories (20 radial spokes, undersampling factor of ~10), respectively. Supporting Information Table S2 summarises the MR undersampling used in all experiments in this study.

MRI in-vivo dataset.

Two healthy volunteer underwent undersampled T1- and T2-weighted 3D whole brain MR scans on a 1.5T Siemens MR scanner using a prototype variable density Cartesian acquisition with spiral profile order (VD-CASPR) with undersampling factors (R) of 3, 9 and 14 (see Ref (32) for more detail on the sampling). The k-space data were acquired using a 16-channel head coil. T1 images were acquired using 3D T1-magnetization-prepared rapid gradient-echo (MPRAGE) with the following parameters: repetition time (TR): 1700 ms, echo time (TE): 2.5 ms, inversion time (TI): 900 ms, echo spacing: 6.24 ms, flip angle: 9 degrees. Acquisition were performed fully sampled and with R = 3, 9, 14, resulting in acquisition times (TA) of 377 sec, 125 sec and 83 sec, respectively. T2 images were acquired using a 3D balanced steady-state free precession sequence with the following parameters: TR: 5000 ms, TE: 2.57 ms, flip angle: 9 degrees. The voxel size of the T1 and T2 images of the first volunteer was set to 1.4×1.4×1.4 mm^3, while for the second one it was set to 1.2×1.2×1.2 mm^3.

PET-MRI in-vivo dataset

A dementia patient underwent a brain PET-MR scan on the Siemens mMR scanner and the following datasets were acquired: i) a 30-min PET scan with an injected activity of 212.82 MBq of [^{18}F]FDG, ii) a Dixon and a UTE MR sequence to generate a 4-tissue class (air, soft tissue, fat and bone) attenuation map for PET attenuation correction, iii) an MPRAGE sequence with the following parameters: 5 channels, TR: 1700 ms, TE: 2.63 ms, TI: 900 ms, echo spacing: 6.24 ms, flip angle: 9 degrees, TA: 142 sec and iv) a 2x-accelerated FLAIR MR sequence with the following parameters: 14 channels, TR: 5000 ms, TE: 395 ms, T1: 1800 ms, echo spacing: 6.24 ms, flip angle: 120 degrees, TA: 397 sec. For PET reconstruction, all correction sinograms were generated using e7 tools (Siemens off-line reconstruction software) and images were reconstructed with PSF modelling using 4.5 mm Gaussian kernels (30) and the scanner's default matrix size as used in our simulations. The k-space of the T1 dataset was retrospectively undersampled using Cartesian trajectories in the phase and slice encoding directions each with a factor of 3, leading to a total acceleration factor R = 9. The k-space of the FLAIR dataset was further retrospectively undersampled in the slice encoding direction by a factor of 3, leading to R = 6. The T1 and FLAIR images were reconstructed in their native matrix and voxel sizes of 512×244×244, 1.05×1.05×1.1 mm^3 and 512×256×160, 0.48×0.48×1.0 mm^3, respectively. Supporting Information Table S2 summarises this experiment.

3.2. Reconstruction methods

The images of both the simulation and in-vivo data were reconstructed as complex valued, however the images shown in the results section are magnitude images. Coil sensitivity maps were calculated by dividing the MR image from each coil by the square root of the sum of squares (SoS) of all the images obtained from all the coils. In this study, the neighbourhood size, $\mathcal{N}_j$, of the quadratic priors in Eq.[2] was set to 5×5×5 for the simulations, whereas for the in-vivo datasets, it was set to 3×3×3 to reduce the computational burden of our reconstructions. The σ and β parameters were set experimentally for all reconstruction set-ups. In order to facilitate and standardize the selection of σ for different images and different datasets, we normalized each image to [0,1] prior to calculation of the Gaussian kernels. Supporting Information Table S3 provides all parameters chosen for the reconstruction of the simulated and real datasets. The PET forward and backprojections were implemented in C++ with GPU acceleration. MR reconstructions were performed in MATLAB (MathWorks, Inc.).

3.3. Evaluation metrics

For the simulations, the performance of different reconstruction methods was quantitatively evaluated compared to a reference image (for PET, the ground truth, for MR, a reconstruction from fully-sampled data), using i) a voxel-level error, defined in Eq.[10], ii) a region-level error, calculated from the mean of the voxel-level errors in a region-of-interest (ROI) and iii) the contrast-to-noise ratio (CNR) for lesions, defined in Eq.[11].

$$\text{Error} = 100 \times \frac{|x_j| - |x_j^{ref}|}{|x_j^{ref}|} \quad [10]$$

$$CNR = 20 \log_{10}\left(\frac{\bar{A}_L - \bar{A}_B}{\overline{SD_B}}\right) \quad [11]$$

where x_j and x_j^{ref} are the jth voxel of a given (complex) image and its corresponding reference image, respectively. $\bar{A}_L$ and $\bar{A}_B$ are the means of the PET activity or MRI intensity in a given lesion and a background region and $\overline{SD_B}$ is the mean standard deviation of activity/intensity in a background region. The background region was defined using 15 ROIs (~10 mm diameter) in different regions of the brain (as shown in Supporting Information Figure S5). Lesions' ROIs were defined by thresholding the simulated PET-MR images at a threshold of 60% of the maximum lesion value. The mean (M) and standard deviation (SD) of voxel-level errors in grey and white matter of each reconstruction were summarized by a root sum of squared (RSS) errors as follows:

$$\text{RSS} = \sqrt{M^2 + SD^2} \quad [12]$$

For in-vivo data, the CNR between the grey and white matter was calculated to evaluate the performance of the algorithms in the absence of a reference image.

4. RESULTS

4.1. Simulations

In Figures 1-2, the reconstruction results of the simulated brain phantom are shown. For visualization, PET images were resampled into MR resolution. Figure 1 shows A) fully sampled SENSE, B) undersampled SENSE, C) undersampled SENSE with TV regularization, D) undersampled SENSE with quadratic regularization weighted using fully sampled T2 image, E) synergistic reconstruction of undersampled T1 and T2 images, F)

synergistic reconstruction of undersampled T1 and PET, and G) synergistic reconstruction of undersampled T1, T2 and PET images. Figures 1 (H-O) show the same results for the T2 image.

Figure 1 shows P) PET ground truth, Q) MLEM reconstruction, R) MAPEM reconstruction with TV regularization, S) MAPEM with quadratic regularization weighted using fully sampled T1 image, T) synergistic reconstruction of undersampled T2 and PET images, U) synergistic reconstruction of undersampled T1 and PET images and V) synergistic reconstruction of undersampled T1, T2 and PET images. Figure 2 show the same results for a sagittal slice containing mismatched PET and T1 lesions. Supporting Information Figure S1-S4 show the same results with error maps and zoomed-in subfigures over mismatches.

The results show that SENSE reconstructions lead to noisy estimates particularly for the T1 image with 6-fold Cartesian undersampling. TV-SENSE reconstructions reduce noise and aliasing artefacts specifically in the T2 image for which the radial undersampling results in incoherent artefacts suitable for sparsity regularization. However, they do not recover all the details, compared to wQ-SENSE which is guided by an artefact-free MR image. In wQ-SENSE reconstructions, there are some residual folding artefacts and suppressed/deformed edges, as shown in the zoomed-in subfigures.

The PET reconstruction results in Figures 1-2 show that the MLEM reconstructions suffer from noise and loss of details, whereas TV-MAPEM notably reduces the noise but induces blurring. The wQ-MAPEM method improves recovery of boundaries however at the cost of inducing tumour-like artefacts for the MR unique lesion and of suppressing and deforming the PET unique lesion (see also Supporting Information Figure S1 and S4). The synergistic reconstruction of the PET and T1 images induces similar artefacts in the PET image, as shown in figures 1-2 (S). The synergistic reconstruction of all datasets together can mitigate these artefacts, however, as shown in Figure 1(V), this algorithm has introduced a false edge through preserving noise at the edge corresponding to the MR unique lesion. Despite this, the proposed method is able to preserve unique lesions. The results in Figures 2(T-V) do however show that the PET lesion's size has slightly shrunk by this method compared to the MLEM and TV-MAPEM methods.

Figure 3 compares the reconstruction methods in terms of mean and standard deviation (SD) of voxel-level errors in grey and white matter for the PET, T1 and T2 images. The numbers above each bar in the figure report RSS errors, as was defined in Eq. 13. The results show that by moving from conventional reconstruction methods to synergistic ones, the mean and SD of the errors are reduced in both the grey and white matter. The conventional MLEM and SENSE methods result in an average RSS error of 13.4% in the grey matter and 16.0% in the white matter, whereas the proposed SynPETMR-T1-T2 methods reduces these errors by more than half. The results show that PET and MR reconstructions using weighted quadratic regularization achieves a better performance than those using TV regularization, however, they are outperformed by the synergistic methods.

Figure 4 shows CNR performance of the reconstructions for PET and T1 lesions. As shown, the MLEM and SENSE reconstructions result in low CNRs, as these methods increase background noise, whereas the TV-MAPEM and TV-SENSE methods result in relatively high CNRs, as the edge-preserving TV regularization suppresses background noise and increases lesion contrast. The wQ-MAPEM and wQ-SENSE methods achieve lower CNR compared to their TV counterparts, because they tend to suppress unique lesions due to mismatches between reconstructed images and their prior images used for guided reconstructions. Synergistic reconstruction results in a comparable and high CNR as they tend to reduce noise and preserve modality-unique lesions.

For simulations, the reconstruction methods were performed with a large number of updates (up to 1200 updates) to ensure their convergence, as summarized in Supporting Information Table S3. In Supporting Information Figure S7, the convergence of the reconstructions is shown in terms of normalized root mean square error (NRMSE) in the whole brain. As expected, MLEM and undersampled SENSE reconstructions give rise to noisy solutions at high iteration numbers and therefore earlier termination is required. The results show that most of the algorithms have converged to a fixed point solution, particularly for the PET and T2 images. Moreover, the synergistically reconstructed data result in the lowest NRMSE in the whole brain.

4.2. In-vivo MRI data

Figures 5-8 compare the synergistic image reconstruction of two in-vivo T1/T2 datasets with conventional zero-filling, SENSE and separate TV-SENSE reconstruction methods for acceleration factors of 3 and 14. Supporting Information Figure S7 and S8 compare the results for all acceleration factors (including 9x) for sagittal slices. Zero-filling images were obtained by filling the unmeasured k-space data with zeros and reconstructed using the conventional sum-of-squares method. Note that in the absence of a fully sampled MR dataset, the wQ-SENSE method was not considered in this experiment. In the VD-CASPR sequence used for this dataset, the sampling of k-space is reduced from the centre towards the periphery of k-space in a spiral and random fashion. Hence, at higher accelerations the reconstructed images suffered from blurring as well as aliasing artefacts. At 3x acceleration, the TV-SENSE and synergistic (i.e. SynMR) methods perform fairly similarly, whereas the zero-filling and SENSE reconstructions show blurring and noise. At higher acceleration, the TV-SENSE reconstructions show blurring and residual artefacts, whereas the synergistic method tends to keep the image quality comparable to the 3x-accelerated images for both the T1 and T2 datasets. The arrows point to the regions with notable differences between the reconstruction methods. Supporting Information Figure S9 compares the CNR performance of the reconstructions between grey and white matter in T1 and T2 images for different acceleration factors. As shown, at each acceleration factor the proposed method achieves the highest CNR thanks to a higher contrast between the grey and white matter and lower background variation.

4.3. In-vivo PET-MR data

Figure 9 and Supporting Information Figure S10 show the conventional and synergistic reconstruction results of the FDG-PET/T1/FLAIR dataset. In this experiment, the reference MR images included the SENSE reconstruction of fully sampled T1 data, and the 2x-accelerated FLAIR datasets. For PET, there was not a reference image. As shown, the MLEM reconstruction suffers from noise and Gibbs ringing artefacts at edges (see arrow in Figure 10). TV reconstructions notably reduce noise and aliasing artefacts apparent in undersampled SENSE reconstructions, however at the expense of resolution and detail loss. The wQ-MAPEM and wQ-SENSE reconstructions guided by reference T1 and FLAIR images improve all modalities by reducing noise and Gibbs/aliasing artefacts, and are able to recover details. Synergistic reconstruction of PET-MR data show that these reconstructions perform fairly comparably to wQ-MAPEM and wQ-SENSE reconstructions while only using undersampled data (9x for T1 and 6x for FLAIR). In addition, as shown by the arrows in Figure 7 and Supporting Information Figure S11, wQ-SENSE has introduced pseudo structures in the FLAIR image due to mismatches between the T1 and FLAIR images, while they are not present in our synergistically reconstructed FLAIR image.

Supporting Information Figure S12 compares CNR between grey and white matter for PET, T1 and FLAIR datasets reconstructed by different methods (not all shown in Figure 9). For PET images, the wQ-MAPEM and SynPETMR reconstructions achieve the highest CNR, while the TV-MAPEM results in the lowest CNR due to reduced contrast between the grey and white matter. For T1 images, the SynMR-T1-FLAIR and SynPETMR-T1 methods achieve a relatively high CNR. The SynPETMR-T1-FLAIR method and wQ-SENSE achieved similar but nonetheless lower CNR, which can be attributed to higher background noise. For the FLAIR images, the results show that almost all of the reconstructions suffer from high background noise and low contrast, leading to negative CNR. However, the results show that the synergistic reconstructions exhibit a relatively better performance.

4.4. Benefits of PET for MR image reconstruction

Our simulation results presented in Figures 3 and 4 show that synergistic reconstructions of PET and T1 MR (i.e. SynPETMR-T1) and that of T1 and T2 (i.e. SynMR-T1-T2) perform quantitatively similar. However, visual inspection of the images, as shown in Supporting Information Figure S13, reveals that the SynPETMR-T1 method is outperformed by SynMR-T1-T2 in recovery of structural details. In order words, the T2 image provides more information for the T1 image reconstruction than for the PET reconstruction. This can be attributed to the fact that the PET data are subject to both noise and detector blurring. Figure 10 compares different synergistic reconstructions of the in-vivo PET-MR dataset. The results show that all three synergistic methods deliver T1 images of similar quality.

4.5. Coupling of image modalities

The key component of synergistic reconstruction is coupling of common boundary information between different image modalities. In the proposed prior, this coupling happens through joint similarity coefficients which are calculated from similarity coefficients of individual images (see Eq. 4). To demonstrate this coupling effect, we compared synergistic T1 and T2 MR reconstructions with the ones guided using individual similarity coefficients, namely “self-guided SENSE”. It is worth mentioning that the difference between self-guided SENSE and wQ-SENSE is that in the former the weights are iteratively calculated from each image itself while in the latter they are precomputed from a prior high-quality image. Supporting Information Figure S14 shows the results of the brain phantom for different reconstruction methods. As shown by the yellow arrow, the wQ-SENSE reconstruction of the T1 image, guided by a fixed fully sampled T2 image, suppresses the lesion, while the self-guided SENSE and synergistic methods preserve this unique lesion. However, the white arrows show that the self-guided method cannot recover the pointed structures whereas the synergistic method is able to fairly recover them due to coupling of T1 and T2 boundary information. Supporting Information Figure S15 also highlights this for synergistic reconstruction of a 14x-accelearted in-vivo MR dataset. As shown by the arrow, for reconstruction of the T2 image, the synergistic reconstruction outperforms the self-guided SENSE reconstruction.

4.6. Comparison with previous methods

In (3), we had previously proposed a generalized joint TV prior with an iterative rescaling of PET and MR gradients using a single global factor. In spite of promising simulation results, this rescaling method is not a robust solution in a practical setting, because for in-vivo PET-MR images the edges have different magnitudes,

thus a single scale factor cannot scale them properly and the joint prior may degenerate to a separate conventional prior. In Supporting Information Figure S16, we compare our previous and current methods using a resolution phantom devised by (1) as a benchmark. As shown, both methods improve the quality of the PET-MR images, especially the joint TV prior, despite large relative intensity differences within the PET-MR data. However, comparing our in-vivo reconstructions in (3) with those in the present work demonstrates that our newly proposed method can effectively harness the synergy of PET-MR data.

We also compared our method with the joint TGV method using the phantom and software publically provided by (2). The results presented in Supporting Information Figure S17 show that both synergistic methods perform similarly for modality-shared edges, but differently for modality-unique lesions. For the PET-unique lesion, the TGV algorithm resulted in the enhancement of the lesion, while our proposed method performs similar to standard MLEM. The TGV enhancement can be attributed to the fact that TGV relies on a total variation prior which is an edge-preserving prior. For this reason, the TGV PET reconstruction appears also non-uniform and patchy. For an MR-unique lesion, the TGV results show that the MR unique lesion has been transferred into the PET image, which is not the case for our method. Our proposed reweighted quadratic prior can be easily extended to a TV one, however, it will make the optimization more complicated as the TV prior is not continuously differentiable, hence either an advanced optimization algorithm is required or a smoothed TV prior (with an additional hyperparameter that controls the degree of edge-preservation).

5. DISCUSSION

This work presents a reconstruction methodology which addresses some of the major challenges of synergistic reconstruction while still exploiting the synergy of PET-MR data. The proposed prior has the following properties: i) It is independent of the intensity ranges of the individual images (i.e. in Figure 1, the T1 image is in the range $[0, 3\times10^4]$ and the PET image is in $[0, 1]$). This is because the kernels ($\mathcal{G}$) defined in Eq. 4 are always in $[0, 1]$, according to the definition of a normal distribution. Therefore, the joint coefficients (ω) are not dominated by the image with larger signal-magnitude (in the above example, the T1 image), because all kernels are normalized and hence will have equal contribution to the joint coefficients. ii) It is scale-invariant, that is, if the intensity range of a given image varies by a factor (i.e. if the T1 image in Figure 1 is scaled from $[0, 3\times10^4]$ to $[0, 3]$), the kernels remain identical. This is because the images are first normalized to $[0, 1]$ and then the kernels are calculated. iii) It is contrast-invariant, that is if the intensity range of a given image is inverted, the kernels remain identical. This because of the square in the exponent of the normal distribution. Note that the property ii) is not because of the nature of the proposed method, but due to the preprocessing step of normalizing the intensity ranges of all input signals. In addition, the property iii) also holds true for any gradient-based coupling such as joint TV or joint TGV reconstruction.

Given the high computational expense of synergistic reconstruction, we heuristically selected the required hyperparameters as summarized in Supporting Information Table S3. For the simulations, one global iteration of synergistic PET-T1-T2 reconstruction, which consisted of two MAPEM iterations for PET, two CG iterations for T1, two CG iterations for T2 (all with neighbourhood sizes of 5×5×5) and their corresponding resampling, took about 8 minutes. Hence, 500 global iterations led to a total reconstruction time of 2.7 days. For in-vivo PET-MR data using the same update schedule as the simulations but with a smaller neighbourhood size of

3×3×3 (to reduce computation time), one global iteration took about 4.3 min (total 11.25 hr for 150 global iterations).

Overall, the performance of synergistic reconstruction depends on the selected hyperparameters, especially the β and σ used in Eqs. (2) and (4). The hyperparameter β controls the level of smoothness while σ controls level of edge-preservation. For a given β, as σ is decreased all the details of the reconstructed images, including noise and undersampling artefacts, will be preserved, since the resulting Gaussian similarity function will be narrower and it will map a smaller weight to intensity differences between voxels. Smaller weights lead to reduced regularization. In our experience, β has a higher impact on the algorithms' performance and varies substantially for different datasets. Neighbourhood size is also another hyperparameter. It has been recommended that larger neighbourhoods lead to better performance of guided reconstruction (33), however in this work we noticed that a neighbourhood size of 3×3×3 is sufficient for both edge identification and faster computation. The update schedule is also another influential hyperparameter. The convergence rate and path of PET and MR reconstructions are different, because the PET system matrix and MR encoding matrix having different condition numbers and use different optimization algorithms. The key component of our methodology is calculation of the mutual similarity coefficients from the current PET and MR image estimates, hence the convergence of PET-MR reconstructions per global iteration is of importance. In particular, if the MR undersampling factor is low, the convergence of the CG algorithm is faster. In this work, updates for PET and MR reconstructions was kept at 2-4 iterations per global iterations. Moreover, convergence of the employed alternating optimization to a global maximum is unknown, as this algorithm was mainly built upon separate PET and MR reconstruction methods. Hence, further work is required to study convergence.

In this work, we used a reweighted quadratic prior instead of a TV or TGV prior. The prior does not introduce additional hyperparameters or constant factors, and thanks to its continuous differentiability there is no need for advanced optimization algorithms, which in turn would add extra hyperparameters to ensure convergence. However, the iterative calculation of weighting coefficients means that the proposed joint objective has multiple local maxima, since different initializations will result in different weighting coefficients and hence different solutions. Hence our objective function is non-convex (strictly speaking non-concave).

In terms of computational complexity compared to previous methods, the added computational load of our algorithm is not substantial as there is no need for optimization with respect to primal and dual variables as used in (2), and no optimization of an augmented Lagrangian problem, as used in (3). The most time consuming stages are the individual regularized PET and MR reconstructions, which are inevitably time consuming. However, the notable added computational burden of our algorithm is the spatial transformations used for mapping different image contrasts to each other before joint calculation of the weighting coefficients. We opted for this extra computational cost in order to reconstruct images in their native resolution. Knoll el al (2) performed reconstruction of PET-MR images in the space of the MR image with high resolution, which can be time consuming especially for PET reconstruction.

Our in-vivo data results in Figure 9 demonstrated that synergistic reconstruction can improve the quality of PET-MR images compared even to guided reconstructions which utilize fully sampled MR images. For synergistic reconstructions, it was found that the gain obtained by PET is more than the little, if any, gain obtained for the MR images from the PET data. This can be mainly attributed to the lower resolution and relatively high noise level of PET data.

In order to be readily comparable to in-vivo datasets, in this study the simulated fully-sampled MR reconstructions were considered as the reference images instead of the ground truth. This is because it is widely regarded within the MR community that the goal is to reconstruct an MR image from undersampled data with a quality comparable to a fully-sampled MR image. In contrast, for PET imaging, there is no such reference image due to the limited acquisition time and the limited resolution of current clinical PET scanners.

In this study, the feasibility and benefits of synergistic multi-contrast MR and PET images was demonstrated. Future work will require evaluation of synergistic reconstruction of non-FDG PET and MR data. In a normal healthy brain, FDG often has a uniform but contrasting uptake in grey and white matter, following the anatomical patterns of the MR images. For non-FDG tracers, the potential merit of synergistic PET-MR reconstruction would still need to be demonstrated, as such tracers might demonstrate a local uptake without any specific anatomical correspondence. Future work should also include synergistic reconstruction of multi-frame dynamic PET data for improved signal to noise ratio of the corresponding image frames.

CONCLUSION

The proposed method aims to exploit the synergy of PET-MR or multi-contrast MR images irrespective of their relative intensity differences and contrasts. Mutually weighted quadratic priors were exploited to promote the simplicity and stability of the resulting algorithm. Our simulations and in-vivo data reconstructions showed that the proposed synergistic reconstruction can considerably improve upon existing TV regularization methods and even prior-image guided reconstructions, particularly in the presence of mismatches between image modalities.

Acknowledgement

This work is supported by the Engineering and Physical Sciences Research Council (EPSRC) under grant EP/M020142/1 and the Wellcome EPSRC Centre for Medical Engineering at King's College London (WT 203148/Z/16/Z). The authors would like to thank Dr Radhouene Neji and Camila Munoz for their consultation on MR image reconstruction. According to EPSRC's policy, all data supporting this study will be openly available at http://dx.doi.org/10.5281/zenodo.1212537

REFERENCES

1. Ehrhardt MJ, Thielemans K, Pizarro L, Atkinson D, Ourselin S, Hutton BF, Arridge SR. Joint reconstruction of PET-MRI by exploiting structural similarity. Inverse Probl. 2014;31:15001.
2. Knoll F, Holler M, Koesters T, Otazo R, Bredies K, Sodickson DK. Joint MR-PET Reconstruction Using a Multi-Channel Image Regularizer. IEEE Trans. Med. Imaging 2017;36:1–16.
3. Mehranian A, Belzunce M, Prieto C, Hammers A, Reader A. Synergistic PET and SENSE MR image reconstruction using joint sparsity regularization. IEEE Trans. Med. Imaging 2017:1–1.
4. Bowsher JE, Hong Yuan, Hedlund LW, et al. Utilizing MRI Information to Estimate F18-FDG Distributions in Rat Flank Tumors. In: IEEE Symposium Conference Record Nuclear Science. Vol. 4. IEEE; pp. 2488–2492.
5. Kazantsev D, Lionheart WRB, Withers PJ, Lee PD. Multimodal Image Reconstruction Using Supplementary

Structural Information in Total Variation Regularization. Sens. Imaging 2014;15:97.
6. Mehranian A, Belzunce MA, Niccolini F, Politis M, Prieto C, Turkheimer F, Hammers A, Reader AJ. PET image reconstruction using multi-parametric anato-functional priors. Phys. Med. Biol. 2017;62:5975.
7. McGibney G, Smith MR, Nichols ST, Crawley A. Quantitative evaluation of several partial Fourier reconstruction algorithms used in MRI. Magn. Reson. Med. 1993;30:51–59.
8. Pruessmann KP, Weiger M, Scheidegger MB, Boesiger P. SENSE: sensitivity encoding for fast MRI. Magn. Reson. Med. 1999;42:952–962.
9. Ying L, Liu B, Steckner MC, Wu G, Wu M, Li S-J. A statistical approach to SENSE regularization with arbitrary *k* -space trajectories. Magn. Reson. Med. 2008;60:414–421.
10. Liu B, King K, Steckner M, Xie J, Sheng J, Ying L. Regularized sensitivity encoding (SENSE) reconstruction using bregman iterations. Magn. Reson. Med. 2009;61:145–152.
11. Candès EJ, Wakin MB, Boyd SP. Enhancing Sparsity by Reweighted ℓ1 Minimization. J. Fourier Anal. Appl. 2008;14:877–905.
12. Otazo R, Candès E, Sodickson DK. Low-rank plus sparse matrix decomposition for accelerated dynamic MRI with separation of background and dynamic components. Magn. Reson. Med. 2015;73:1125–1136.
13. Kreutz-Delgado K, Murray JF, Rao BD, Engan K, Lee T-W, Sejnowski TJ. Dictionary learning algorithms for sparse representation. Neural Comput. 2003;15:349–396.
14. Ehrhardt MJ, Betcke MM. Multi-Contrast MRI Reconstruction with Structure-Guided Total Variation. SIAM J. Imaging Sci. 2016;9:1084–1106.
15. Birns S, Kim B, Ku S, Stangl K, Needell D. A Practical Study of Longitudinal Reference Based Compressed Sensing for MRI. CoRR, abs/1608.04728. 2016.
16. Weizman L, Eldar YC, Bashat D Ben. Compressed sensing for longitudinal MRI: An adaptive-weighted approach. Med Phys 2015;42:5195.
17. Weizman L, Eldar YC, Eilam A, Londner S, Artzi M, Ben Bashat D. Fast reference based MRI. In: 2015 37th Annual International Conference of the IEEE Engineering in Medicine and Biology Society (EMBC). IEEE; 2015. pp. 7486–7489.
18. Peng X, Du H-Q, Lam F, Babacan SD, Liang Z-P. Reference-driven MR image reconstruction with sparsity and support constraints. In: 2011 IEEE International Symposium on Biomedical Imaging: From Nano to Macro. IEEE; 2011. pp. 89–92.
19. Chavarrías C, Abascal JFPJ, Montesinos P, Desco M. Exploitation of temporal redundancy in compressed sensing reconstruction of fMRI studies with a prior-based algorithm (PICCS). Med. Phys. 2015;42:3814–3821.
20. Huang J, Chen C, Axel L. Fast multi-contrast MRI reconstruction. Magn. Reson. Imaging 2014;32:1344–1352.
21. Weizman L, Mota JFC, Song P, Eldar YC, Rodrigues MRD. Joint Multicontrast MRI Reconstruction. Signal Process. with Adapt. Sparse Struct. Represent. 2017.
22. Chen C, Li Y, Huang J. Calibrationless Parallel MRI with Joint Total Variation Regularization. 2013:106–114.
23. Bilgic B, Goyal VK, Adalsteinsson E. Multi-contrast reconstruction with Bayesian compressed sensing. Magn. Reson. Med. 2011;66:1601–1615.
24. Holler M, Huber RM, Knoll F. Coupled regularization with multiple data discrepancies. Inverse Probl.

inpress 2018.
25. Ramani S, Fessler JA. Parallel MR Image Reconstruction Using Augmented Lagrangian Methods. IEEE Trans. Med. Imaging 2011;30:694–706.
26. De Pierro AR. A modified expectation maximization algorithm for penalized likelihood estimation in emission tomography. IEEE Trans. Med. Imaging 1995;14:132–137.
27. Wang G, Qi J. Penalized likelihood PET image reconstruction using patch-based edge-preserving regularization. IEEE Trans. Med. Imaging 2012;31:2194–2204.
28. Pruessmann KP, Weiger M, Börnert P, Boesiger P. Advances in sensitivity encoding with arbitrary k-space trajectories. Magn. Reson. Med. 2001;46:638–651.
29. Collins DL, Zijdenbos AP, Kollokian V, Sled JG, Kabani NJ, Holmes CJ, Evans AC. Design and construction of a realistic digital brain phantom. IEEE Trans. Med. Imaging 1998;17:463–468.
30. Belzunce, M. A., Mehranian, A., Chalampalakis, Z., Reader AJ. Evaluation of shift-invariant image-space PSFs for the Biograph mMR PET Scanner. PSMR Conf. Rec. 2017.
31. Guerquin-Kern M, Lejeune L, Pruessmann KP, Unser M. Realistic analytical phantoms for parallel magnetic resonance imaging. IEEE Trans. Med. Imaging 2012;31:626–636.
32. Bustin A, Ginami G, Cruz G, Correia T, Ismail T, Rashid I, Neji R, Botnar R PC. Five-Minute Whole-Heart Coronary MRA with Sub-millimeter Isotropic Resolution, 100% Respiratory Scan Efficiency and 3D-PROST Reconstruction. Magn Reson Med 2018, doi 10.1002/mrm.27354.
33. Vunckx K, Atre A, Baete K, Reilhac A, Deroose CM, Van Laere K, Nuyts J. Evaluation of three MRI-based anatomical priors for quantitative PET brain imaging. IEEE Trans. Med. Imaging 2012;31:599–612.

Figure captions

Figure 1. Reconstruction results for the simulated T1, T2 and PET data, showing T1 unique lesion. Captions categorise the reconstructions in different groups. (A,H) SENSE reconstruction of fully sampled data (C,J) SENSE reconstruction of undersampled data, (C,K) TV-SENSE reconstruction of undersampled data, (D,L) wQ-SENSE reconstruction of undersampled T1 and T2 data weighted using fully sampled T2 and T1 images, respectively, (E,M) synergistic reconstruction of undersampled T1 and T2 data, (F,U) synergistic reconstruction of undersampled T1 and PET data, (N,T) synergistic reconstruction of undersampled T2 and PET data and (G,O,V) synergistic reconstruction of undersampled T1, T2 and PET data. (P) PET ground truth, (Q) MLEM, (R) TV-MAPEM, (S) wQ-MAPEM weighted using fully sampled T1 image. Note that the PET images have been resampled to T1 MR resolution.

Figure 2. Same as figure 1, but for a sagittal slice showing T1 and PET unique lesions.

Figure 3. Mean (horizontal bold lines) and standard deviation (vertical bars) of voxel-wise errors in grey and white matter for different reconstruction methods together with their root sum of squared errors (numbers shown above each bar).

Figure 4. CNR results for the separate and synergistic MR and PET-MR reconstructions.

Figure 5. Synergistic reconstruction of the prospectively undersampled T1 (left) and T2 (right) datasets for a healthy volunteer. Acceleration factor and resulting acquisition time (in minutes and seconds) of each scan are shown.

Figure 6. Zoomed-in of Figure 5.

Figure 7. Same as Figure 5 for another healthy volunteer.

Figure 8. Zoomed-in of Figure 7.

Figure 9 Synergistic PET-MR image reconstruction of the PET-MR dataset in comparison with the conventional and separate reconstruction methods.

Figure 10 Comparison of different synergistic PET-MR image reconstruction of the in-vivo PET-MR dataset.

Supporting Information captions

Supporting Information Table S1. Abbreviations and descriptions of the reconstruction algorithms used for the simulated and real datasets in this study.

Supporting Information Table S2. Reconstruction set-ups for k-space undersampling of different MR image contrasts of the simulation and clinical datasets

Supporting Information Table S3. Parameters used for the reconstruction of the simulated and in-vivo datasets using the studied reconstruction methods.

Supporting Information Figure S1. Same as Figure 1, but with added voxel-wise error maps.

Supporting Information Figure S2. Zoomed-in of Figure 1.

Supporting Information Figure S3. Same as Figure 2, but with added voxel-wise error maps.

Supporting Information Figure S4. Zoomed-in of Figure 2.

Supporting Information Figure S5. Background ROIs used for calculation of CNR in the simulated brain phantom.

Supporting Information Figure S6. Convergence of the reconstruction methods in terms of normalized root mean square error (NRMSE) in the whole brain for each image update of the simulated PET, T1 and T2 MR datasets.

Supporting Information Figure S7. Synergistic reconstruction of the prospectively undersampled T1 (left) and T2 (right) datasets for the first healthy volunteer. The acceleration factor and resulting acquisition time (in minutes and seconds) of each scan are shown.

Supporting Information Figure S8. Synergistic reconstruction of the prospectively undersampled T1 (left) and T2 (right) datasets for the second healthy volunteer. Acceleration factor and resulting acquisition time (in minutes and seconds) of each scan are shown.

Supporting Information Figure S9. CNR between grey and white matter of the T1 and T2 images of the in-vivo MR datasets.

Supporting Information Figure S10. Same as Figure 9 but for a sagittal slice. The arrow indicates Gibbs artefacts in the PET MLEM reconstruction.

Supporting Information Figure S11. Zoomed in from Figure 9. The arrows point to structural artefacts induced by T1-guidance of the FLAIR reconstruction, (i.e. wQ-SENSE).

Supporting Information Figure S12. CNR between grey and white matter of the FDG-PET, T1 and FLAIR images of the in-vivo PET-MR dataset.

Supporting Information Figure S13. Comparison of different synergistic reconstructions of the simulated PET-MR dataset for synergistic reconstruction of T1 and T2 (SynMR-T1-T2), PET and T1 (SynPETMR-T1), and PET, T1 and T2 (SynPETMR-T1-T2). Comparison of SynMR-T1-T2 and SynPET-MR-T1 shows that the T1 image has been improved more when synergistically reconstructed with the T2 image than the PET image (see arrows). Synergistic reconstruction of all data together (in SynPETMR-T1-T2) is beneficial for all reconstructions.

Supporting Information Figure S14. Illustration of the coupling effect of common boundary information between T1 and T2 datasets through their synergistic reconstruction. Compared to self-guided reconstruction, the synergistic one is able to recover more structural details and at the same time preserve unique lesions that are otherwise suppressed by wQ-SENSE.

Supporting Information Figure S15. Same as Supporting Figure 14, but for the volunteer MR scan #2.

Supporting Information Figure S16. Performance comparison of the proposed synergistic reconstruction method with our previous work in (3), using a joint total variation prior generalized using a non-convex potential function, on the resolution phantom proposed by Ehrhardt et al (1) for the '*radial 20*' simulation set-up.

Supporting Information Figure S17. Performance comparison of our proposed synergistic algorithm with the synergistic TGV one proposed in Ref (2). In this comparison, the code and simulated dataset were obtained from Ref. (24)

Supporting Materials

Supporting Information Table S1. Abbreviations and descriptions of the reconstruction algorithms used for the simulated and real datasets in this study.

Modality	Algorithm	Description
PET	MLEM	Eq.[5]
	TV-MAPEM	MAPEM recon. using TV prior and the one-step-late algorithm (33).
	wQ-MAPEM	MAPEM recon. using quadratic prior weighted by a fully sampled MR image, Eq.[5-6].
MR	SENSE	SENSE recon. of fully or undersampled MR data using the CG algorithm (28).
	TV-SENSE	SENSE recon. of undersampled data using TV prior and alternating direction method of multipliers algorithm (3).
	wQ-SENSE	SENSE recon. of undersampled data using a quadratic prior weighted by a fully sampled MR image and the CG algorithm.
	SynMR-T1-T2(FLAIR†)	Synergistic recon. of undersampled T1 and undersampled T2 (or FLAIR) images using steps 2 and 3b of proposed algorithm (Table 1)
PET-MR	SynPETMR-T1(T2)	Synergistic recon. of PET and undersampled T1(or T2) images
	SynPETMR-T1-T2 (FLAIR)	Synergistic recon. of PET, undersampled T1 and undersampled T2 (or FLAIR) images

† FLAIR : Fluid attenuated inversion recovery

Supporting Information Table S2. Reconstruction set-ups for k-space undersampling of different MR image contrasts of the simulation and clinical datasets

Simulated PET-MR data	In-vivo MR dataset for	In-vivo PET-MR dataset
T1, Cartesian under-sampling in phase encoding direction, R = 6 T2, Radial under-sampling with stack of 20 spokes (R ~10)	Both T1 and T2 datasets VD-CASPR with under-sampling factors of 3, 9 and 14	T1, Cartesian under-sampling in phase (R = 3) and slice encoding (R = 3) directions, total R = 9 FLAIR, Cartesian under-sampling in phase (R = 2) and slice encoding (R = 3) directions, total R = 6

Supporting Information Table S3. Parameters used for the reconstruction of the simulated and in-vivo datasets using the studied reconstruction methods.

	Reconstruction method	No. global iterations	PET			T1			T2/FLAIR		
			No. MAPEM iterations (P_{iter})	β	σ	No. SENSE-CG iterations (M_{iter})	β	σ	No. SENSE-CG iterations	β	σ
Simulation	*PET*: MLEM	–	1000	0	–	–	–	–	–	–	–
	PET: TV-MAPEM	–	1000	100	–	–	–	–	–	–	–
	PET: wQ-MAPEM	–	1000	6×10^5	0.08	–	–	–	–	–	–
	T1: Fully sampled	–	–	–	–	150	–	–	–	–	–
	T1: SENSE	–	–	–	–	150	–	–	–	–	–
	T1: TV-SENSE	600	–	–	–	2	15	–	–	–	–
	T1: wQ- SENSE	–	–	–	–	1000	0.05	0.01	–	–	–
	T2: Fully sampled	–	–	–	–	–	–	–	150	–	–
	T2: SENSE	–	–	–	–	–	–	–	150	–	–
	T2: TV-SENSE	600	–	–	–	–	–	–	2	15	–
	T2: wQ-SENSE	–	–	–	–	–	–	–	1000	2	0.05
	SynMR-T1-T2	500	–	–	–	2	0.3	0.03	2	0.3	0.03
	SynPETMR-T1	500	2	6×10^5	0.1	–	–	–	2	0.4	0.02
	SynPETMR-T1-T2	500	2	6×10^5	0.1	2	0.4	0.02	2	0.4	0.02
Real MR data : Volunteer #1	*T1*: SENSE (3x)	–	–	–	–	5	–	–	–	–	–
	T1: SENSE (9x)	–	–	–	–	5	–	–	–	–	–
	T1: SENSE (14x)	–	–	–	–	5	–	–	–	–	–
	T1: TV-SENSE (3x)	20	–	–	–	2	0.001	–	–	–	–
	T1: TV-SENSE (9x)	20	–	–	–	2	0.001	–	–	–	–
	T1: TV-SENSE (14x)	20	–	–	–	2	0.001	–	–	–	–
	T2: SENSE (3x)	–	–	–	–	5	–	–	–	–	–
	T2: SENSE (9x)	–	–	–	–	5	–	–	–	–	–
	T2: SENSE (14x)	–	–	–	–	5	–	–	–	–	–
	T2: TV-SENSE (3x)	20	–	–	–	2	0.001	–	–	–	–
	T2: TV-SENSE (9x)	20	–	–	–	2	0.001	–	–	–	–
	T2: TV-SENSE (14x)	20	–	–	–	2	0.001	–	–	–	–
	SynMR-T1-T2 (3x)	20	–	–	–	4	20	0.03	4	20	0.03
	SynMR-T1-T2 (9x)	20	–	–	–	8	15	0.03	8	15	0.03
	SynMR-T1-T2 (14x)	20	–	–	–	10	7	0.03	10	7	0.03
Real MR data: Volunteer #2	*T1*: SENSE (3x)		–	–	–	5	–	–	–	–	–
	T1: SENSE (9x)		–	–	–	5	–	–	–	–	–
	T1: SENSE (14x)		–	–	–	5	–	–	–	–	–
	T1: TV-SENSE (3x)	10	–	–	–	2	0.1	–	–	–	–
	T1: TV-SENSE (9x)	10	–	–	–	2	0.1	–	–	–	–
	T1: TV-SENSE (14x)	10	–	–	–	2	0.05	–	–	–	–
								–		–	–
	T2: SENSE (3x)		–	–	–	–	–	–	5	–	–
	T2: SENSE (9x)		–	–	–	–	–	–	5	–	–
	T2: SENSE (14x)		–	–	–	–	–	–	5	–	–
	T2: TV-SENSE (3x)	10	–	–	–	–	–	–	2	0.2	–
	T2: TV-SENSE (9x)	10	–	–	–	–	–	–	2	0.2	–
	T2: TV-SENSE (14x)	10	–	–	–	–	–	–	2	0.05	–
	SynMR-T1-T2 (3x)	20	–	–	–	4	15	0.03	4	15	0.03
	SynMR-T1-T2 (9x)	20	–	–	–	4	15	0.03	4	15	0.03
	SynMR-T1-T2 (14x)	20	–	–	–	4	30	0.03	4	30	0.03
Real PET-MR data	*PET*: MLEM	–	300	–	–	–	–	–	–	–	–
	PET: TV-MAPEM	–	300	100	–	–	–	–	–	–	–
	PET: wQ-MAPEM	–	300	5×10^4	0.1	–	–	–	–	–	–
	T1: Fully sampled	–	–	–	–	150	–	–	–	–	–
	T1: SENSE	–	–	–	–	150	–	–	–	–	–
	T1: TV-SENSE	150	–	–	–	2	300	–	–	–	–
	FLAIR: SENSE (2x)	–	–	–	–	–	–	–	150	–	–
	FLAIR: SENSE (6x)	–	–	–	–	–	–	–	150	–	–
	FLAIR: TV-SENSE	150	–	–	–	–	–	–	2	300	–
	SynMR-T1-FLAIR	150	–	–	–	2	10	0.04	2	8	0.005
	SynPETMR-T1	150	2	3×10^4	0.1	2	3	0.015	–	–	–
	SynPETMR-T1-FLAIR	150	2	3×10^4	0.2	2	3	0.015	2	5	0.006

Note: For MAPEM-TV, a smoothed TV with smoothing parameter of $\delta = 0.01$ was used. The OSL algorithm was then used for optimization. For SENSE-TV reconstructions, an exact TV prior was used. For simulated and real PET-MR data the penalty parameter of the ADMM algorithm was set to $\rho = 1$, while for the in-vivo MR data it was set to $\rho = 0.1$. See (3) for more details of both the OSL and ADMM algorithms.

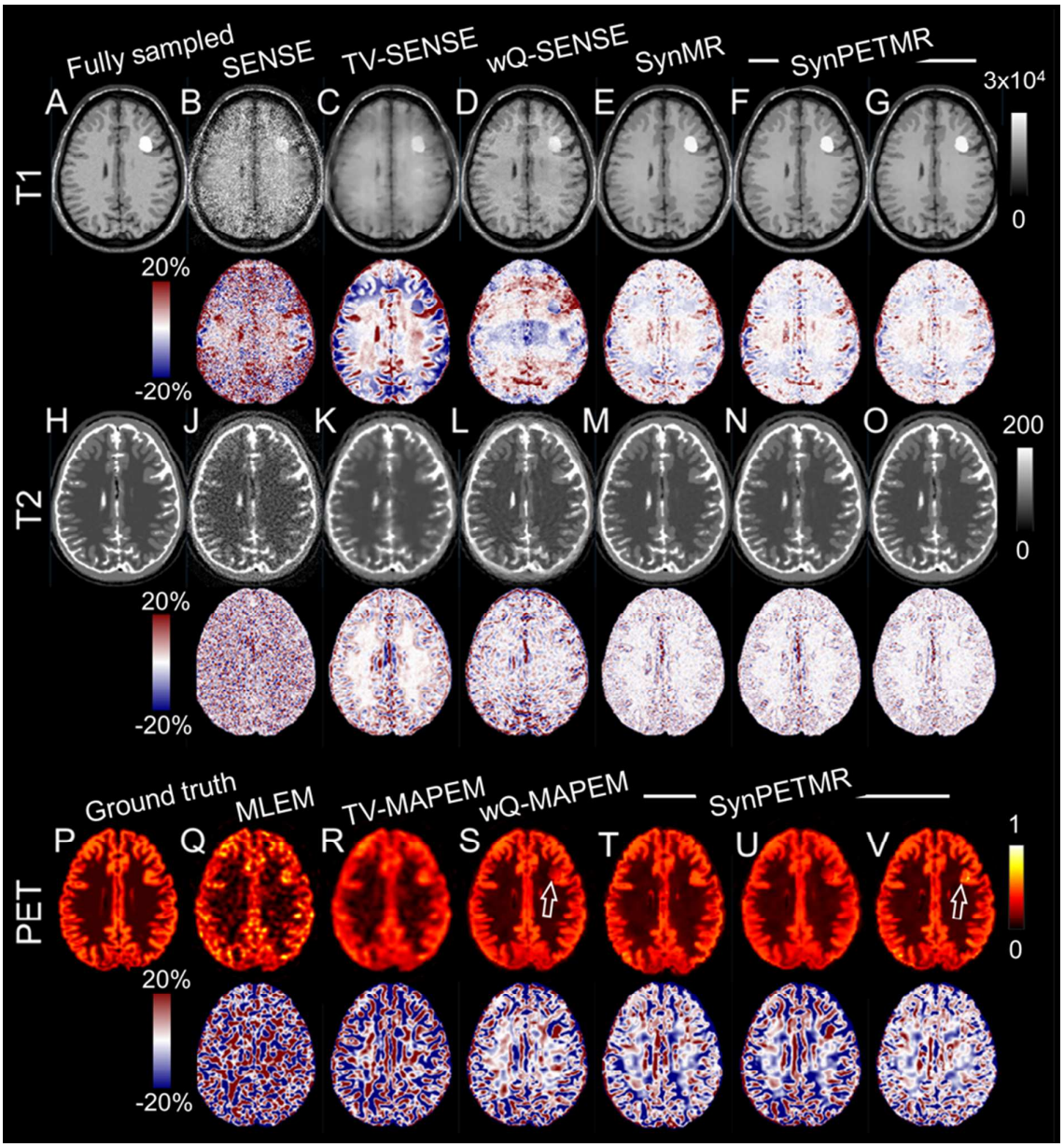

Supporting Information Figure S1. Same as Figure 1, but with added voxel-wise error maps.

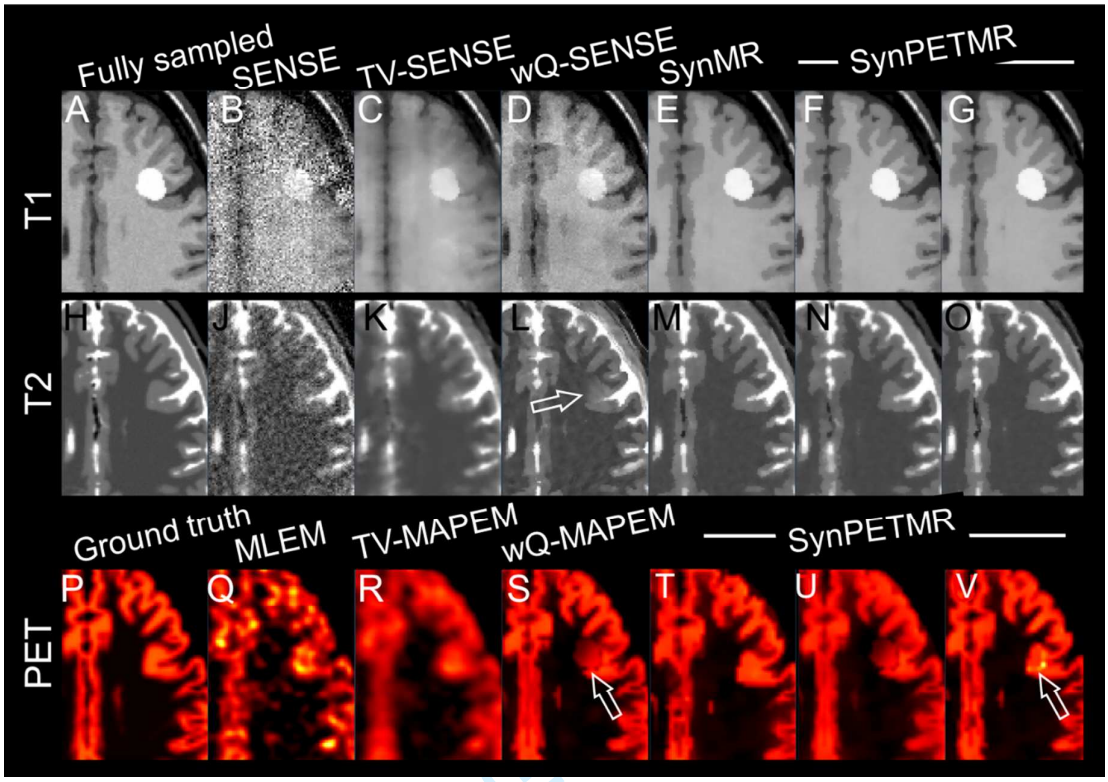

Supporting Information Figure S2. Zoomed-in of Figure 1.

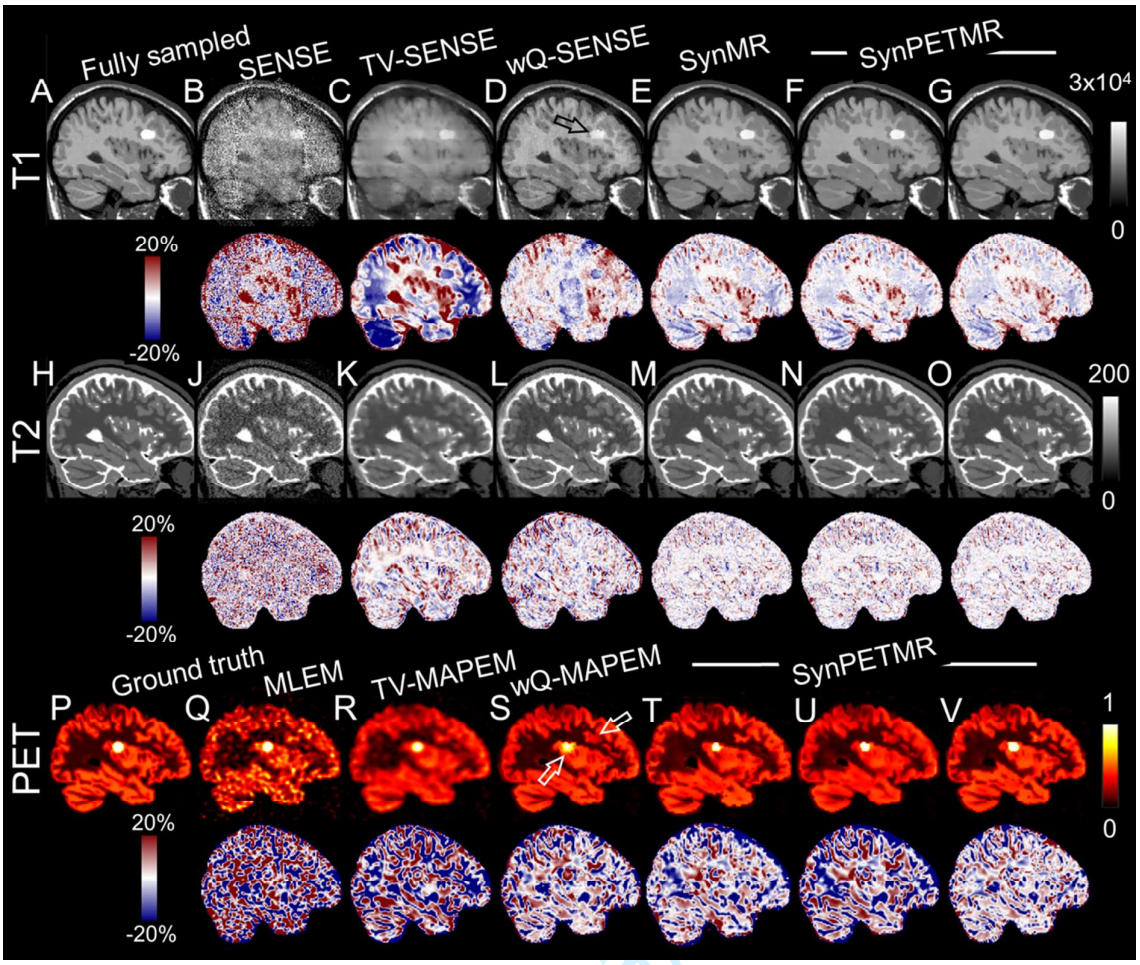

Supporting Information Figure S3. Same as Figure 2, but with added voxel-wise error maps.

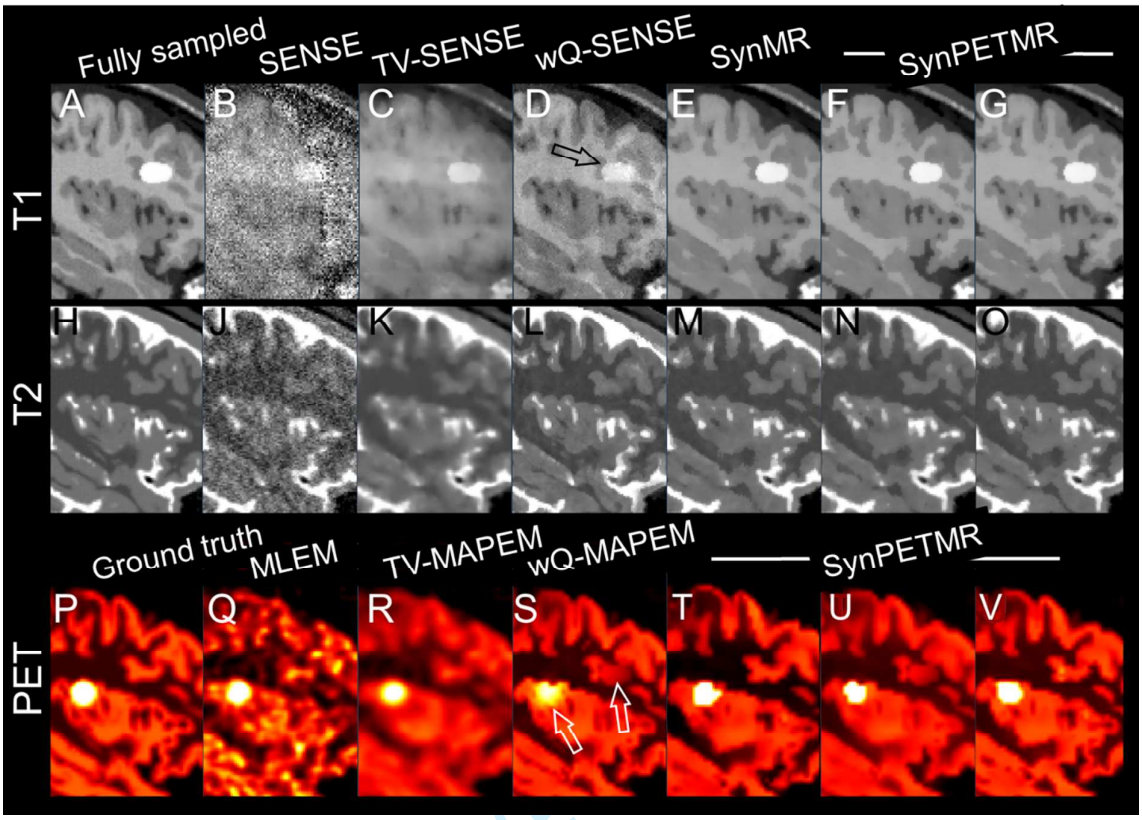

Supporting Information Figure S4. Zoomed-in of Figure 2.

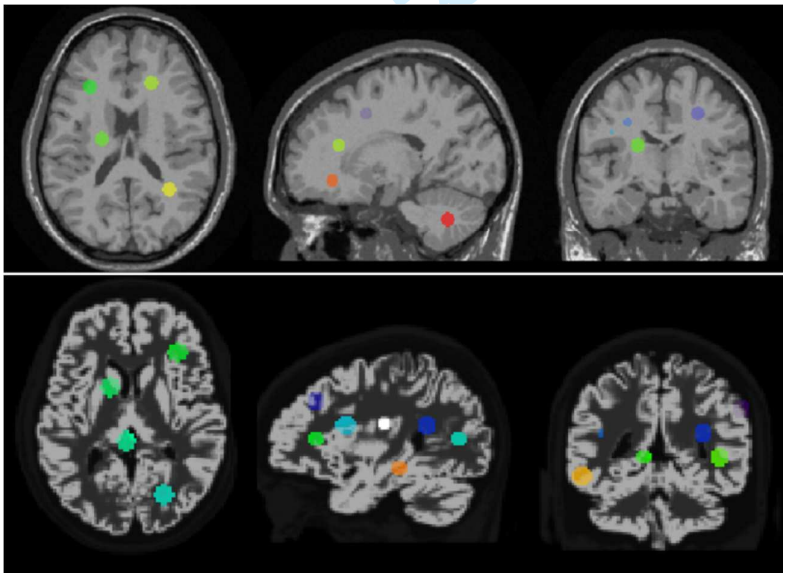

Supporting Information Figure S5. Background ROIs used for calculation of CNR in the simulated brain phantom.

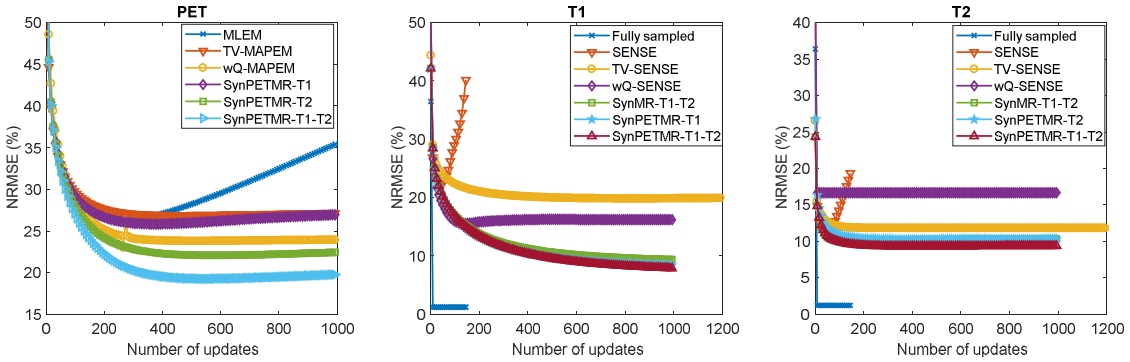

Supporting Information Figure S6. Convergence of the reconstruction methods in terms of normalized root mean square error (NRMSE) in the whole brain for each image update of the simulated PET, T1 and T2 MR datasets.

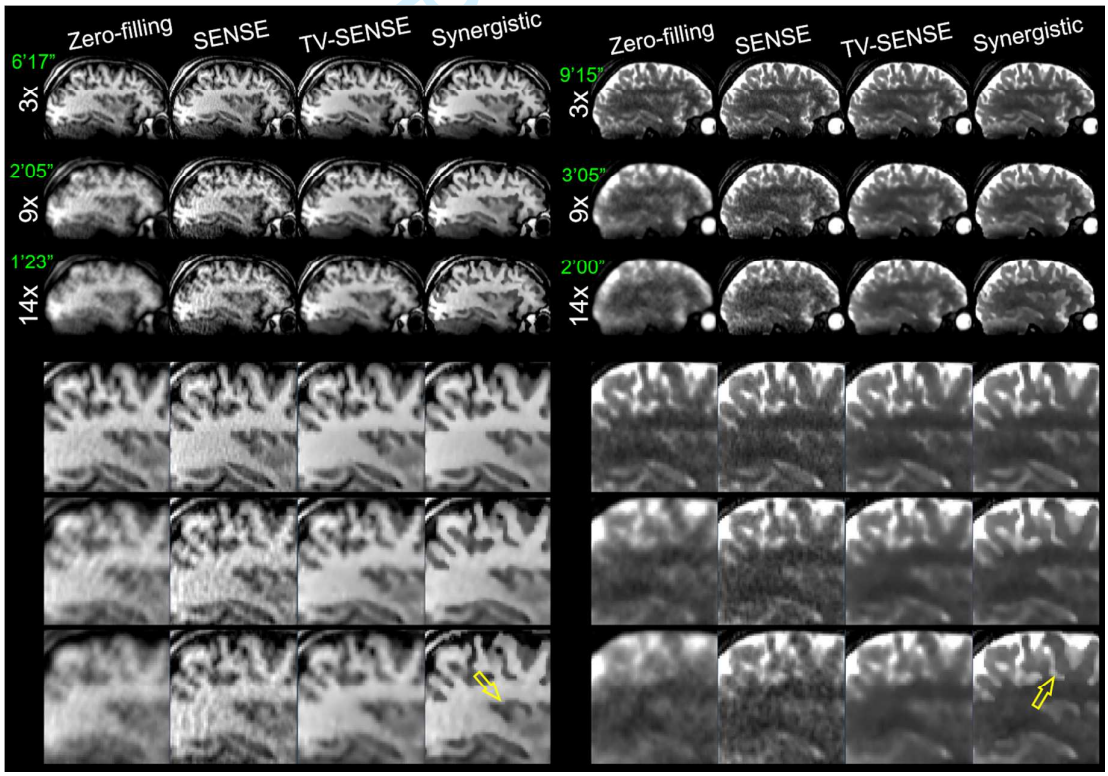

Supporting Information Figure S7. Synergistic reconstruction of the prospectively undersampled T1 (left) and T2 (right) datasets for the first healthy volunteer. The acceleration factor and resulting acquisition time (in minutes and seconds) of each scan are shown.

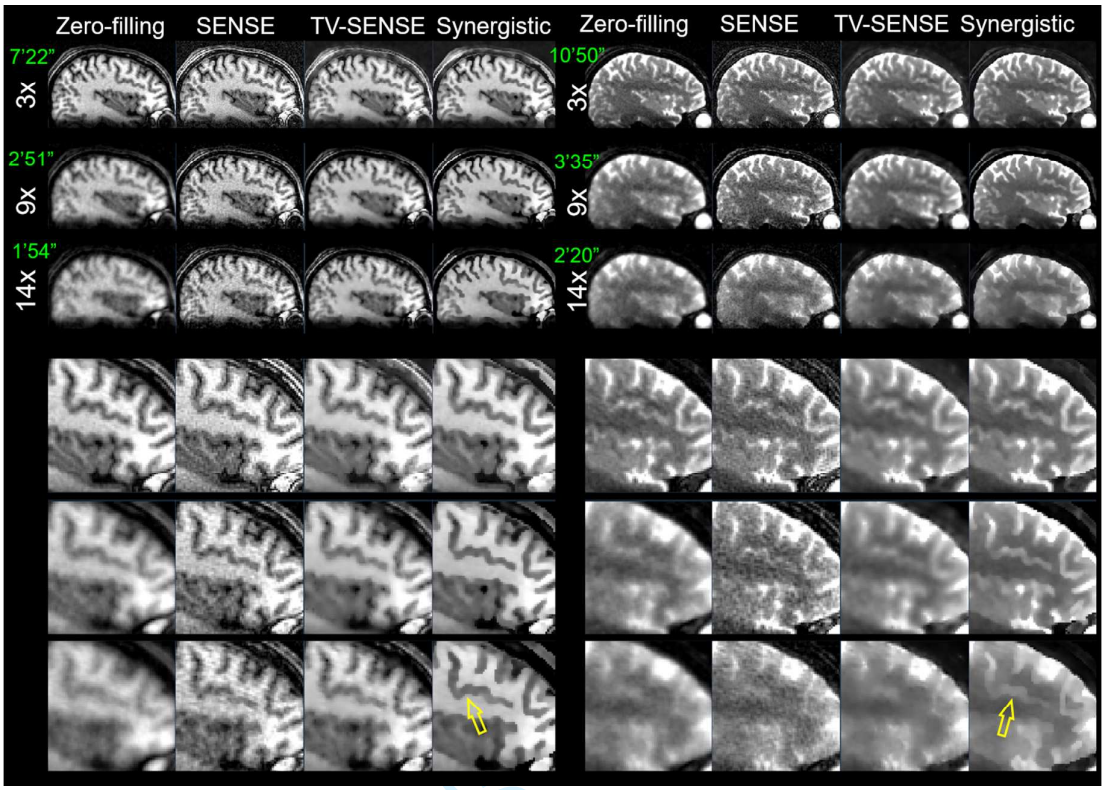

Supporting Information Figure S8. Synergistic reconstruction of the prospectively undersampled T1 (left) and T2 (right) datasets for the second healthy volunteer. Acceleration factor and resulting acquisition time (in minutes and seconds) of each scan are shown.

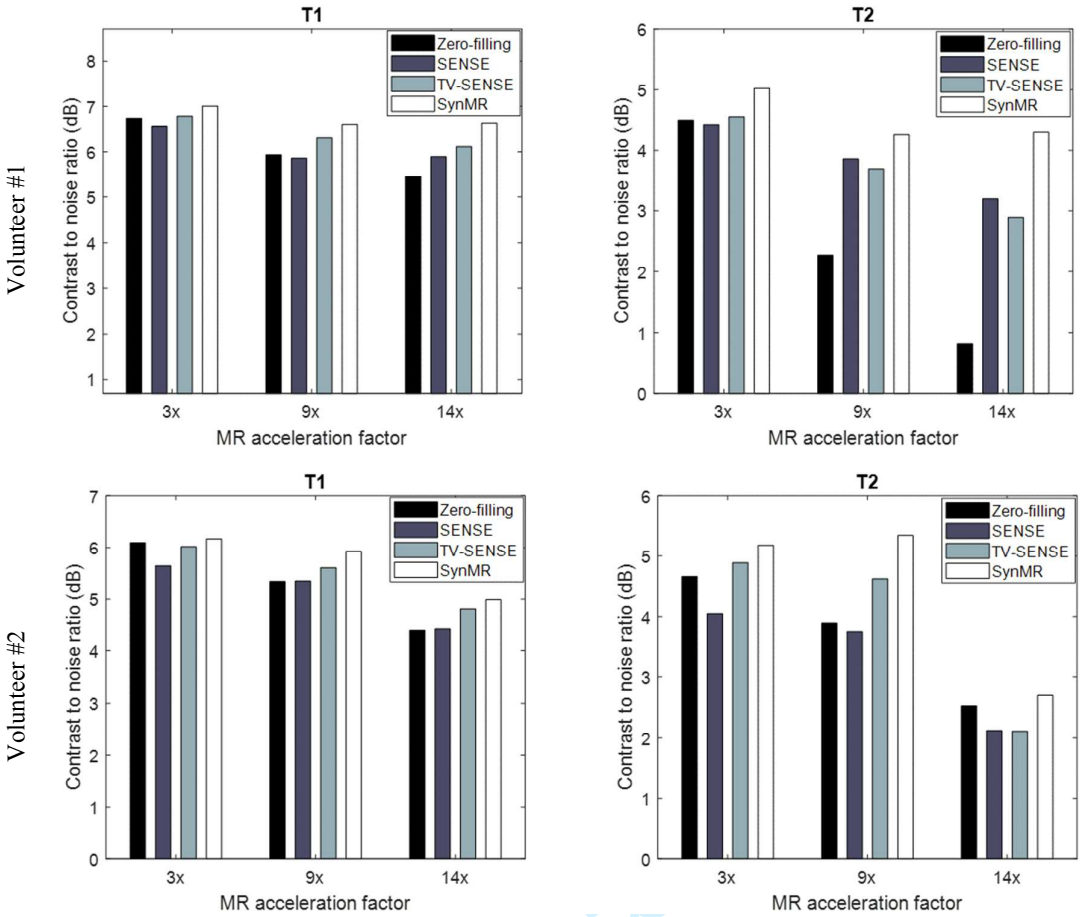

Supporting Information Figure S9. CNR between grey and white matter of the T1 and T2 images of the in-vivo MR datasets.

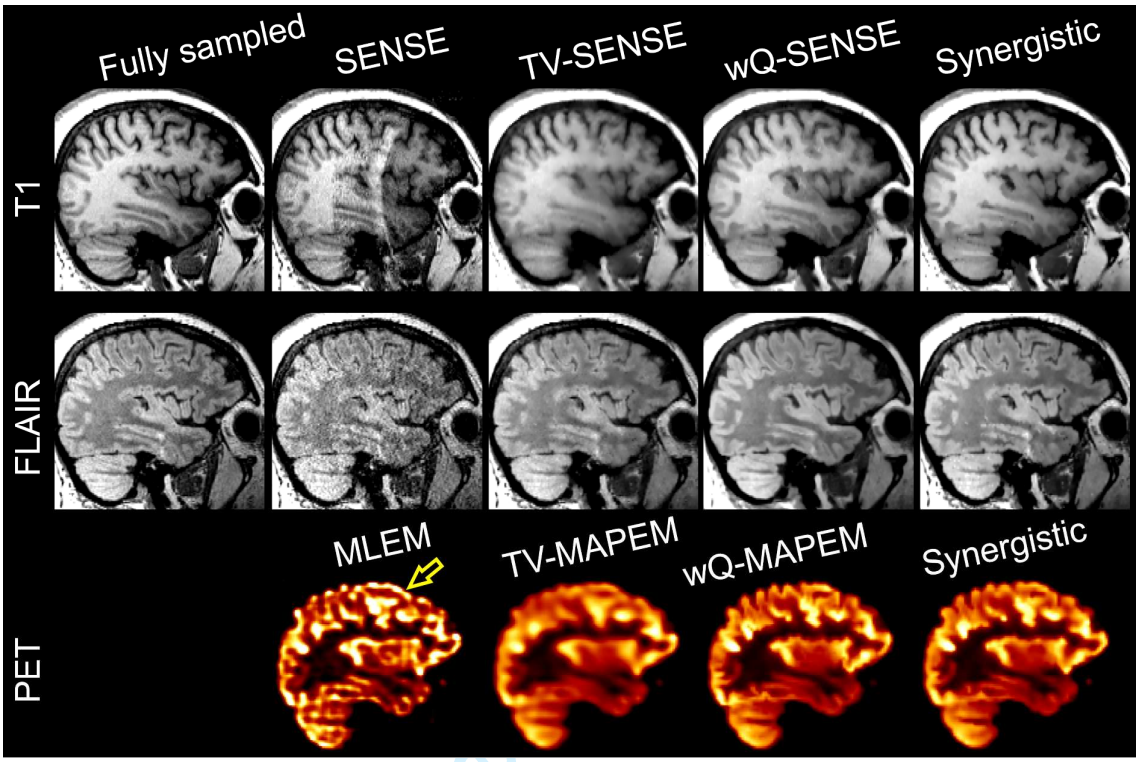

Supporting Information Figure S10. Same as Figure 9 but for a sagittal slice. The arrow indicates Gibbs artefacts in the PET MLEM reconstruction.

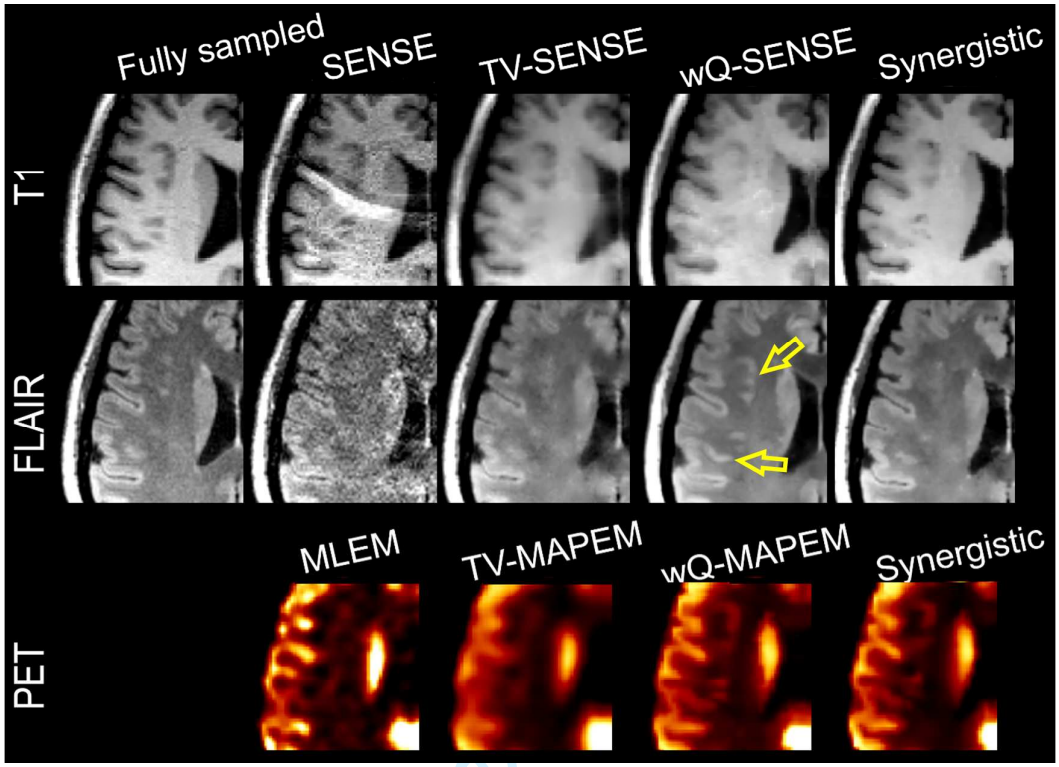

Supporting Information Figure S11. Zoomed in from Figure 9. The arrows point to structural artefacts induced by T1-guidance of the FLAIR reconstruction, (i.e. wQ-SENSE).

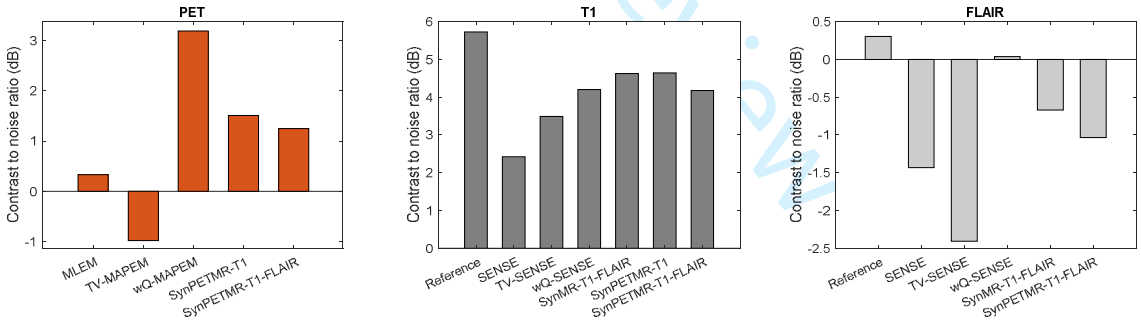

Supporting Information Figure S12. CNR between grey and white matter of the FDG-PET, T1 and FLAIR images of the in-vivo PET-MR dataset.

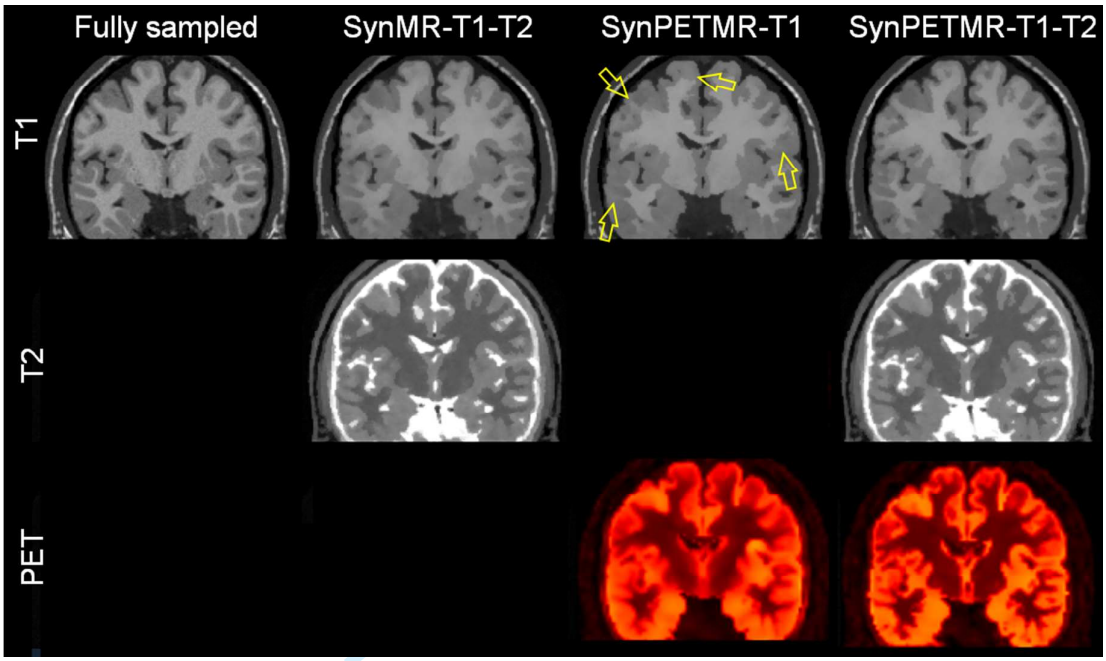

Supporting Information Figure S13. Comparison of different synergistic reconstructions of the simulated PET-MR dataset for synergistic reconstruction of T1 and T2 (SynMR-T1-T2), PET and T1 (SynPETMR-T1), and PET, T1 and T2 (SynPETMR-T1-T2). Comparison of SynMR-T1-T2 and SynPET-MR-T1 shows that the T1 image has been improved more when synergistically reconstructed with the T2 image than the PET image (see arrows). Synergistic reconstruction of all data together (in SynPETMR-T1-T2) is beneficial for all reconstructions.

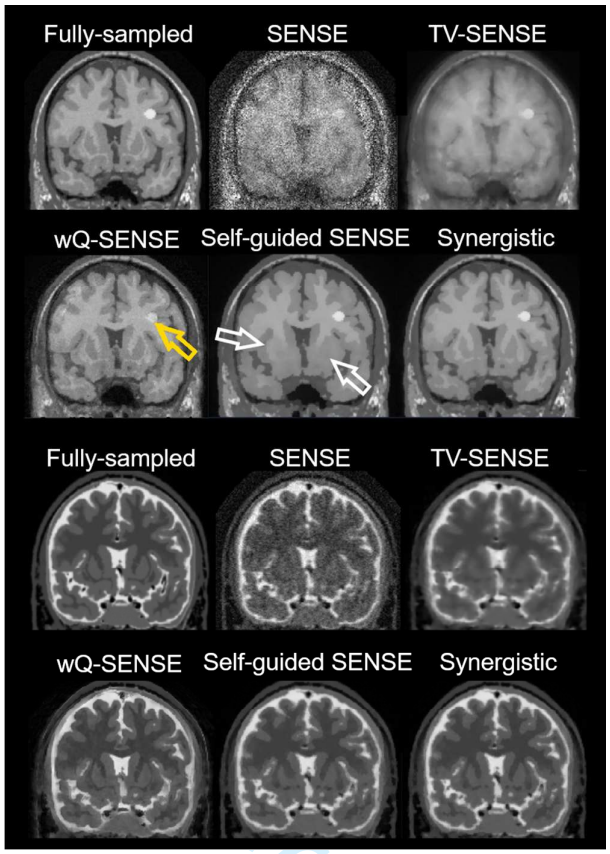

Supporting Information Figure S14. Illustration of the coupling effect of common boundary information between T1 and T2 datasets through their synergistic reconstruction. Compared to self-guided reconstruction, the synergistic one is able to recover more structural details and at the same time preserve unique lesions that are otherwise suppressed by wQ-SENSE.

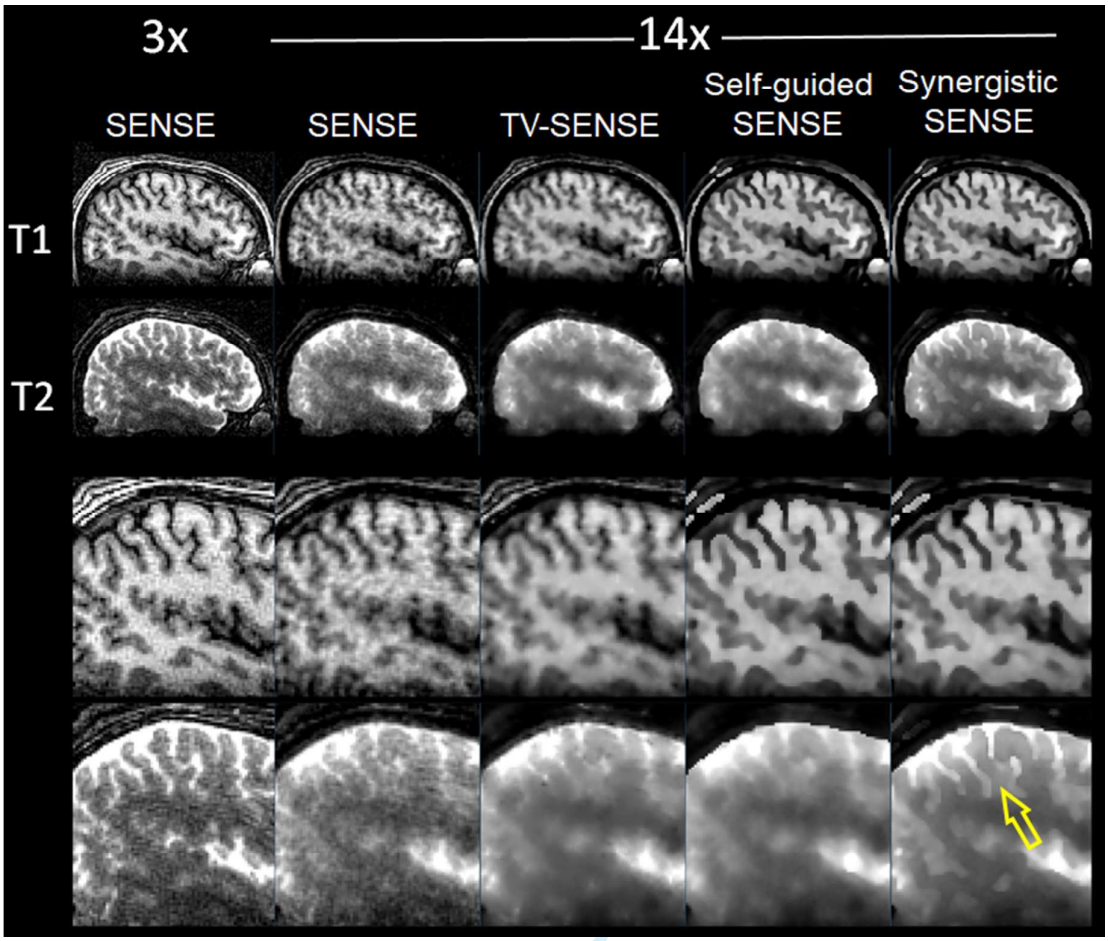

Supporting Information Figure S15. Same as Supporting Figure 14, but for the volunteer MR scan #2.

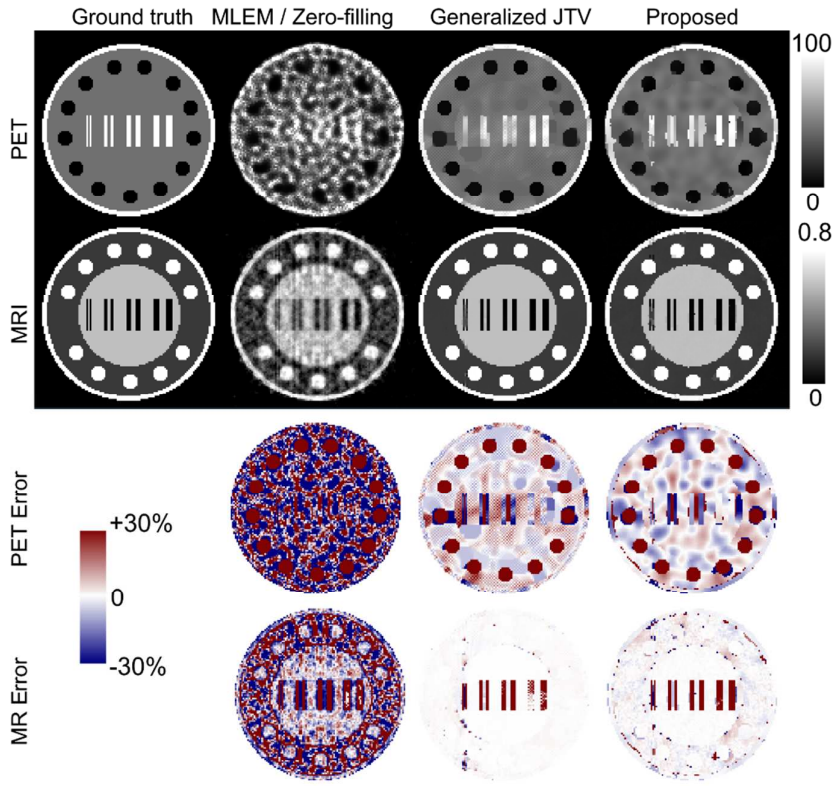

Supporting Information Figure S16. Performance comparison of the proposed synergistic reconstruction method with our previous work in (3), using a joint total variation prior generalized using a non-convex potential function, on the resolution phantom proposed by Ehrhardt et al (1) for the '*radial 20*' simulation set-up.

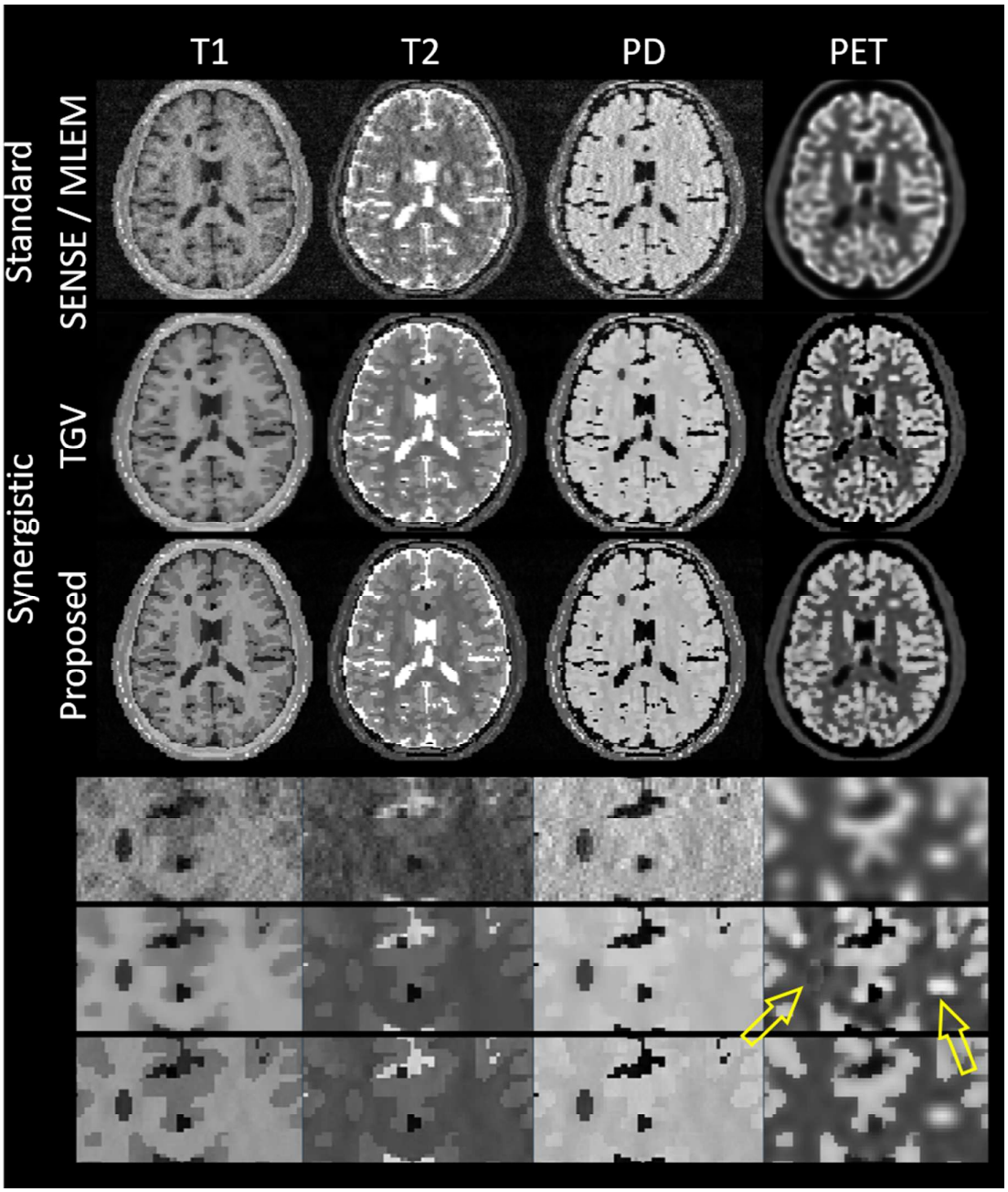

Supporting Information Figure S17. Performance comparison of our proposed synergistic algorithm with the synergistic TGV one proposed in Ref (2). In this comparison, the code and simulated dataset were obtained from Ref. (24)

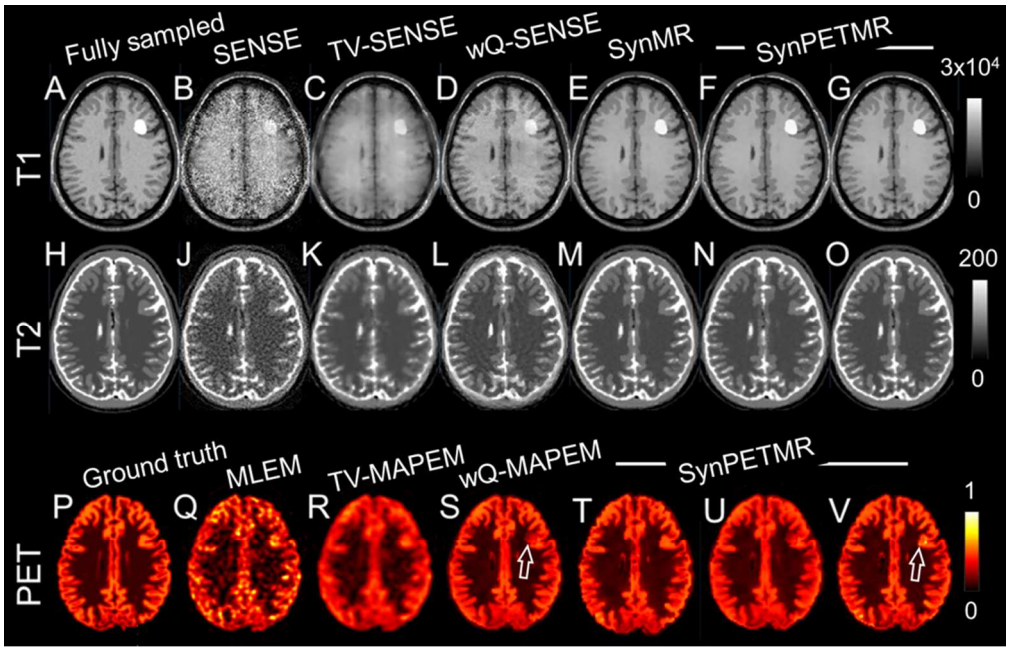

Figure 1. Reconstruction results for the simulated T1, T2 and PET data, showing T1 unique lesion. Captions categorise the reconstructions in different groups. (A,H) SENSE reconstruction of fully sampled data (C,J) SENSE reconstruction of undersampled data, (C,K) TV-SENSE reconstruction of undersampled data, (D,L) wQ-SENSE reconstruction of undersampled T1 and T2 data weighted using fully sampled T2 and T1 images, respectively, (E,M) synergistic reconstruction of undersampled T1 and T2 data, (F,U) synergistic reconstruction of undersampled T1 and PET data, (N,T) synergistic reconstruction of undersampled T2 and PET data and (G,O,V) synergistic reconstruction of undersampled T1, T2 and PET data. (P) PET ground truth, (Q) MLEM, (R) TV-MAPEM, (S) wQ-MAPEM weighted using fully sampled T1 image. Note that the PET images have been resampled to T1 MR resolution.

87x56mm (300 x 300 DPI)

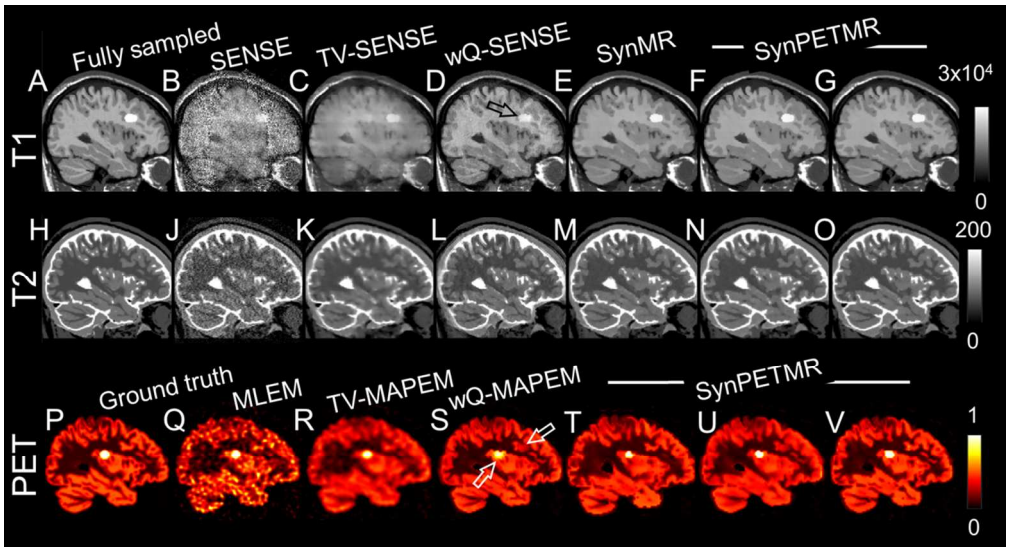

Figure 2. Same as figure 1, but for a sagittal slice showing T1 and PET unique lesions.

113x61mm (300 x 300 DPI)

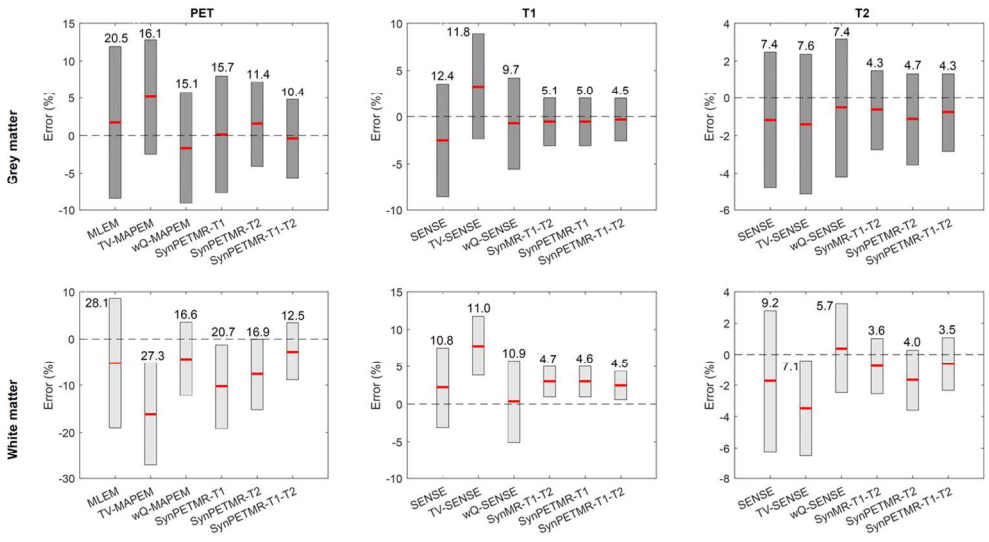

Figure 3. Mean (horizontal bold lines) and standard deviation (vertical bars) of voxel-wise errors in grey and white matter for different reconstruction methods together with their root sum of squared errors (numbers shown above each bar).

59x31mm (600 x 600 DPI)

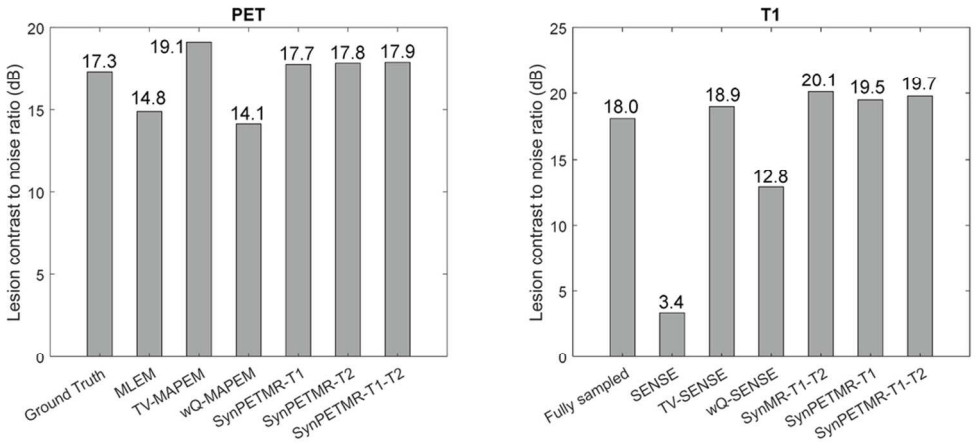

Figure 4. CNR results for the separate and synergistic MR and PET-MR reconstructions.

48x22mm (600 x 600 DPI)

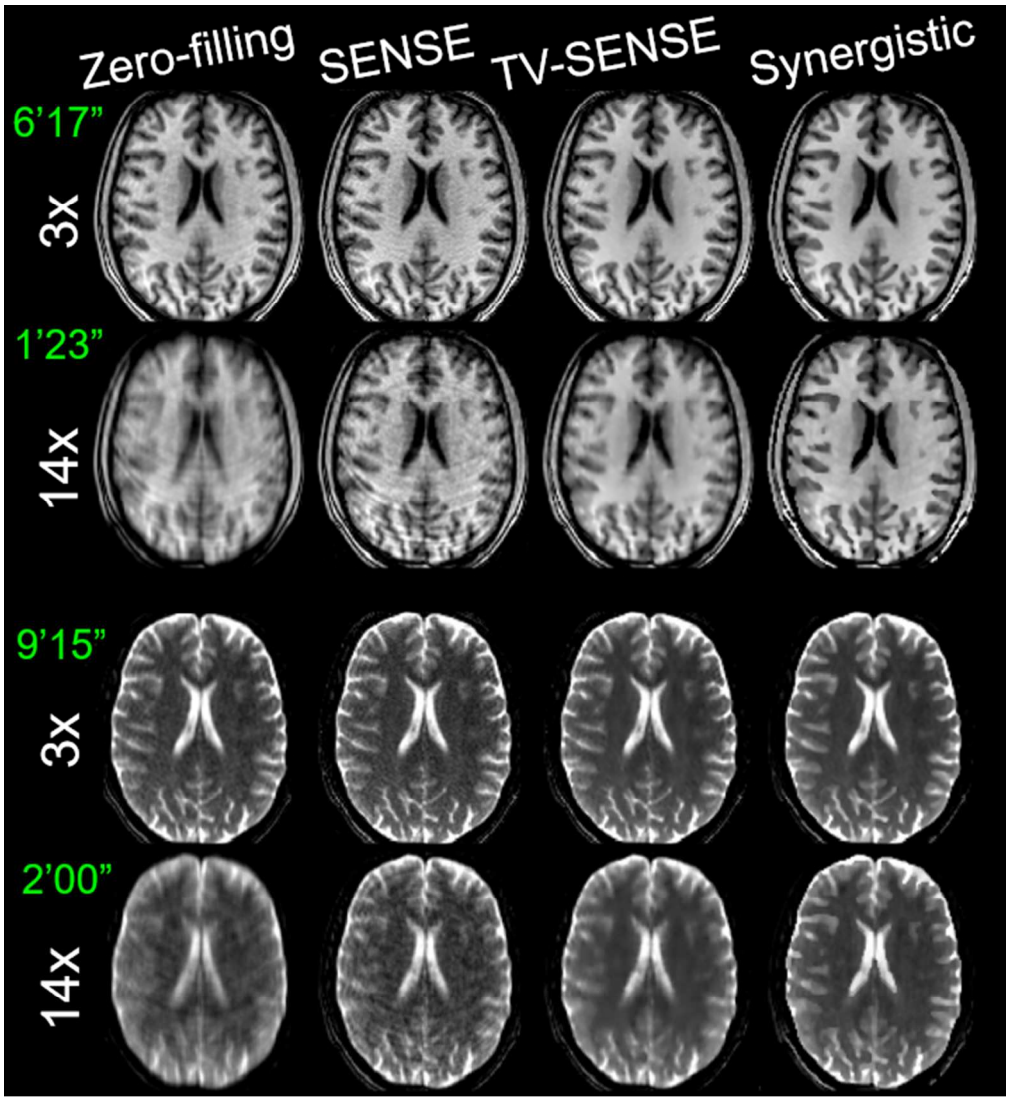

Figure 5. Synergistic reconstruction of the prospectively undersampled T1 (left) and T2 (right) datasets for a healthy volunteer. Acceleration factor and resulting acquisition time (in minutes and seconds) of each scan are shown.

60x65mm (300 x 300 DPI)

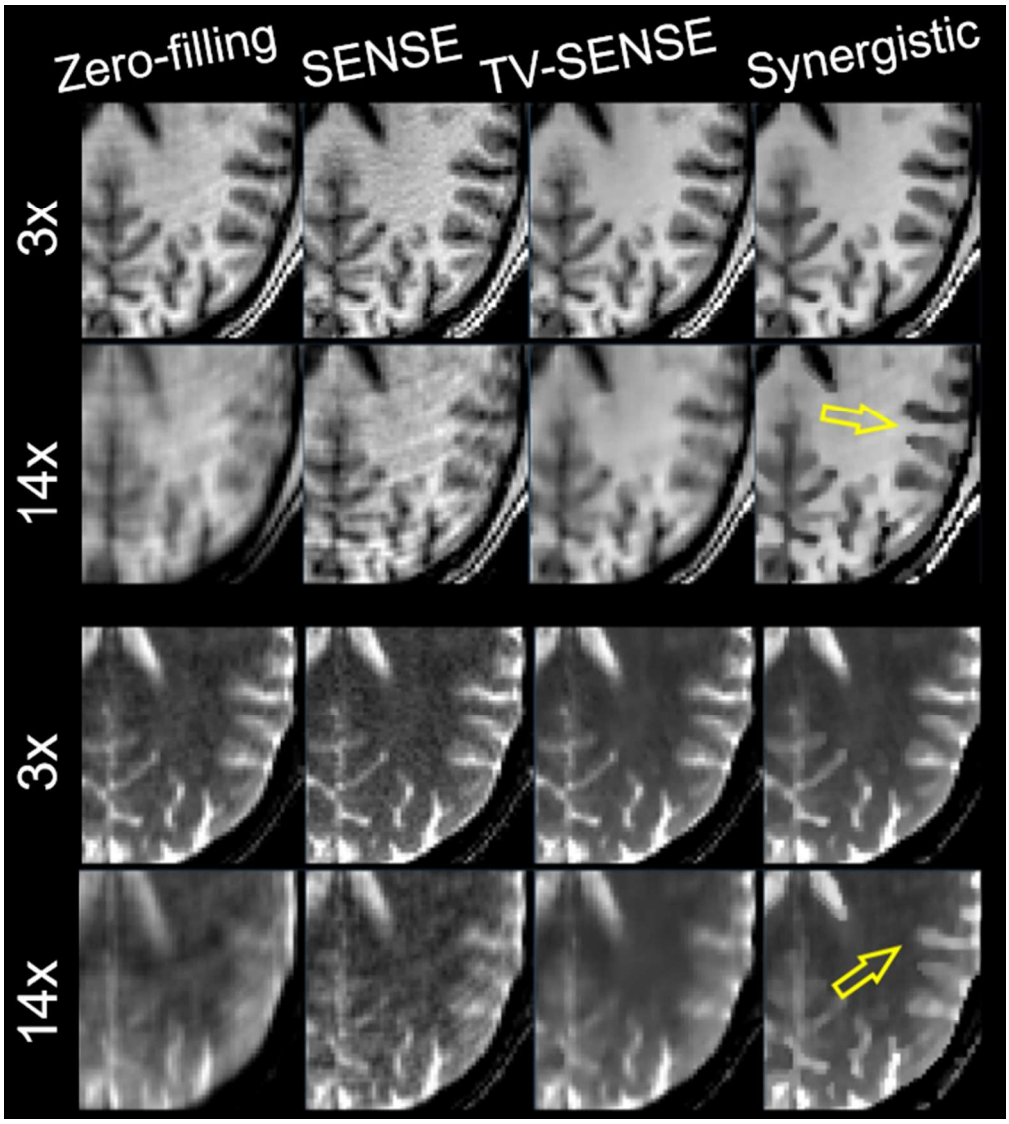

Figure 6. Zoomed-in of Figure 5.

58x65mm (300 x 300 DPI)

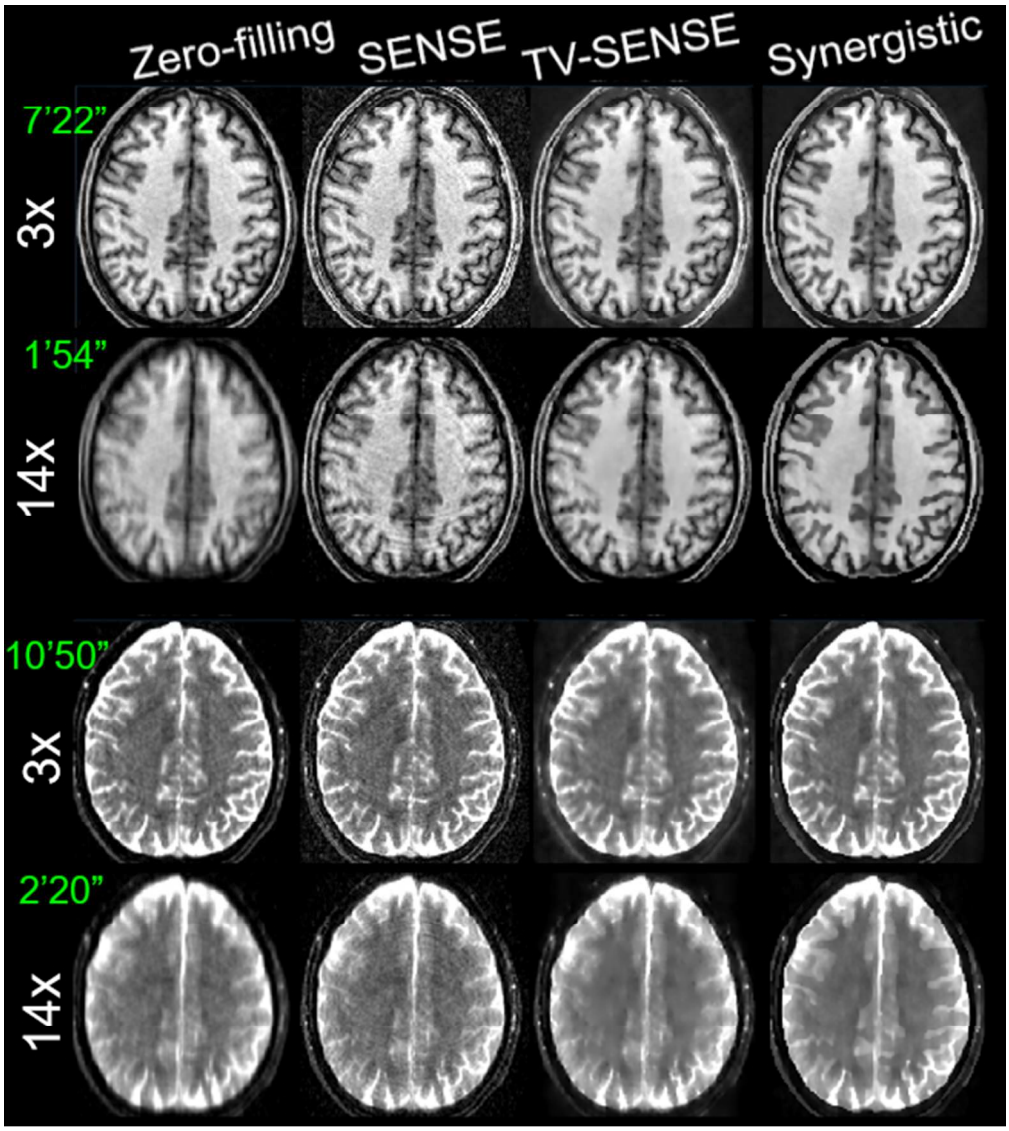

Figure 7. Same as Figure 5 for another healthy volunteer.

55x61mm (300 x 300 DPI)

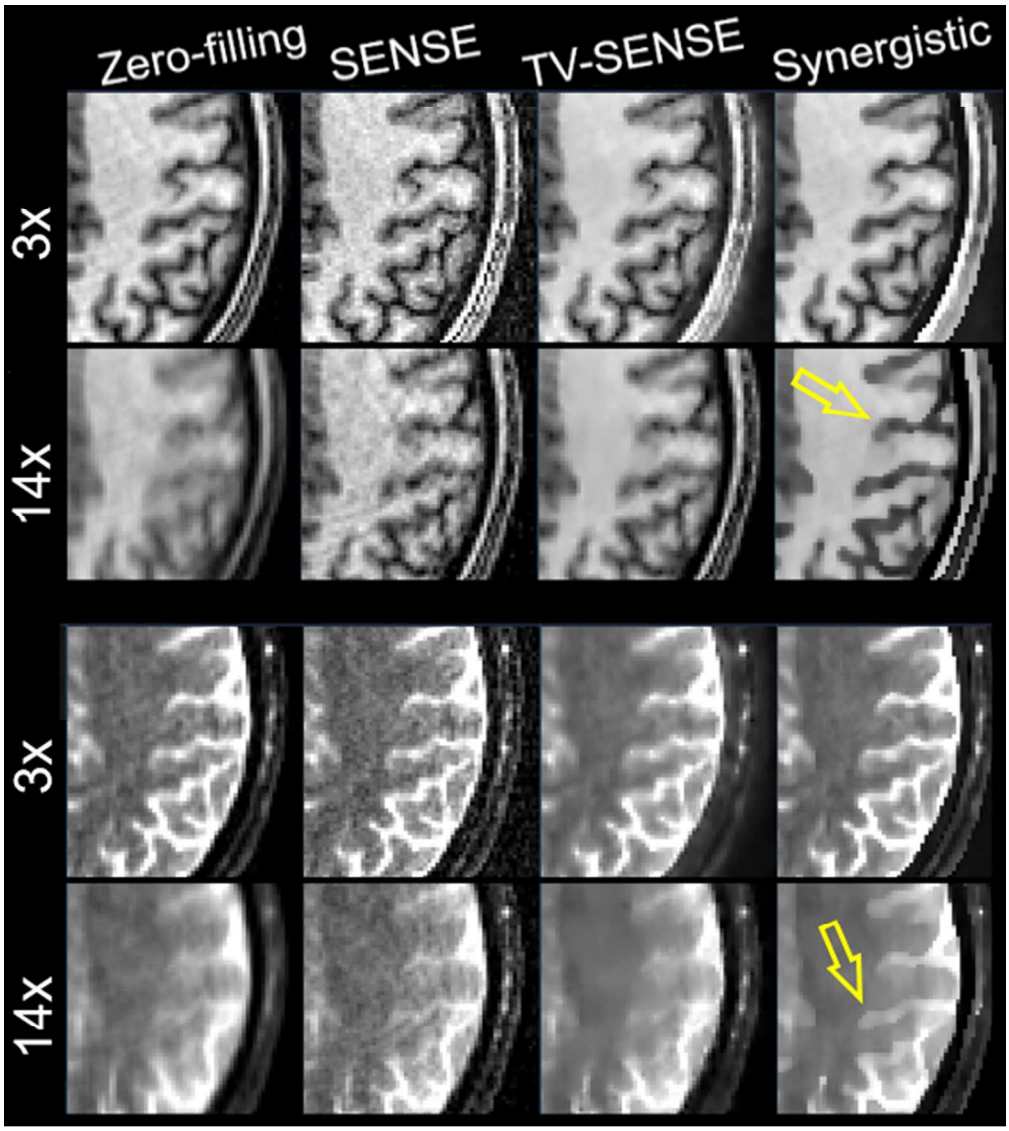

Figure 8. Zoomed-in of Figure 7.

54x60mm (300 x 300 DPI)

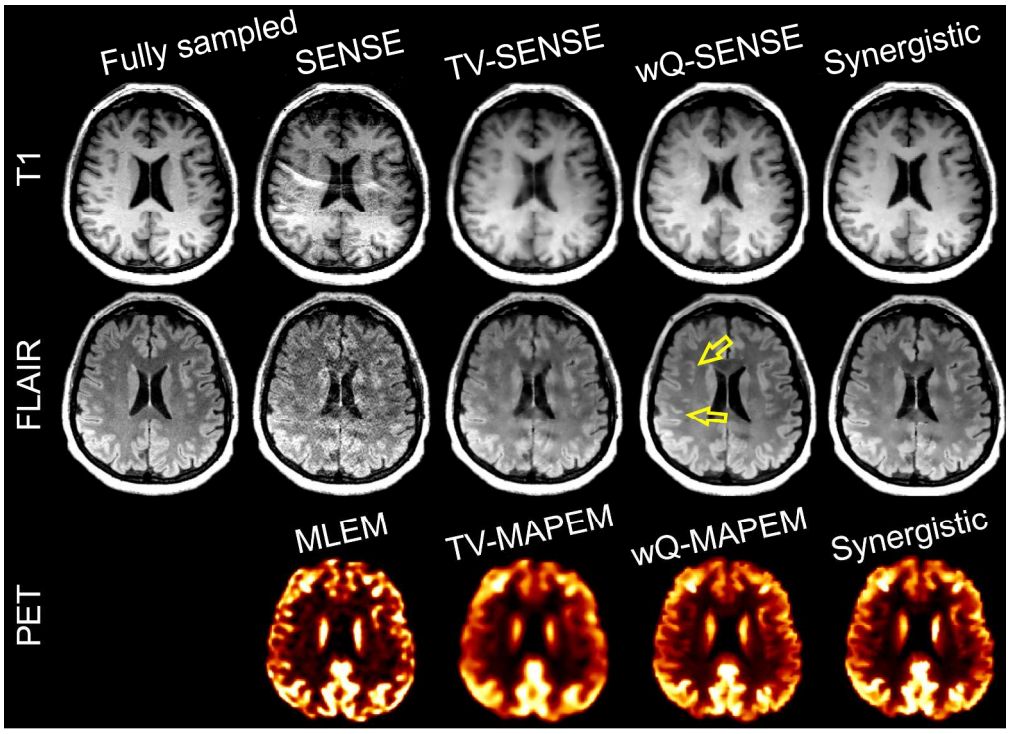

Figure 9 Synergistic PET-MR image reconstruction of the PET-MR dataset in comparison with the conventional and separate reconstruction methods.

238x172mm (300 x 300 DPI)

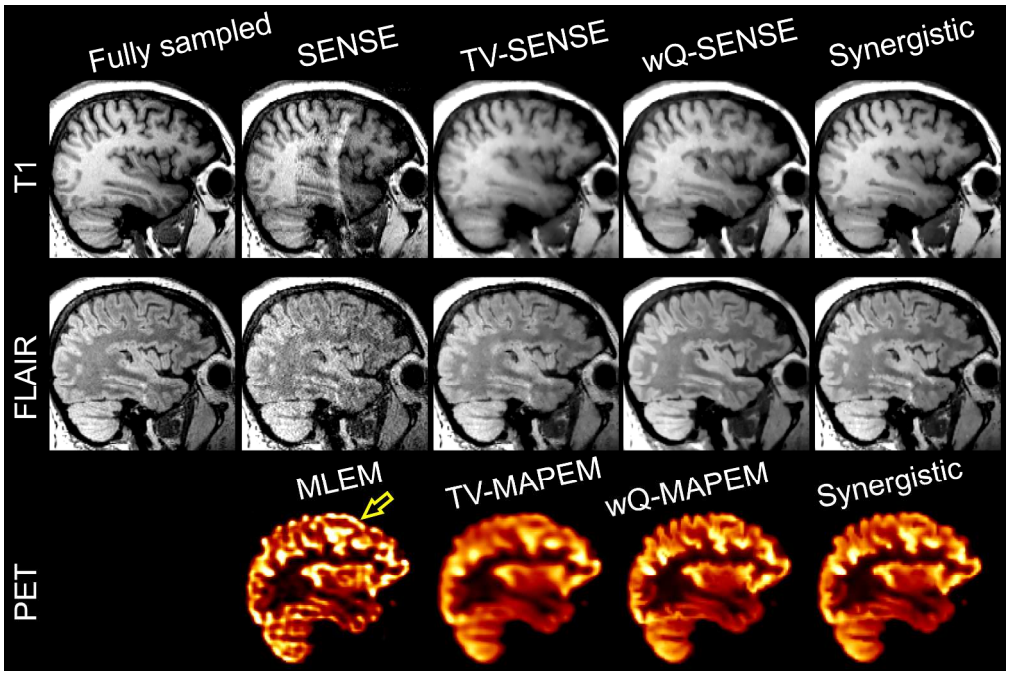

Figure 10 Comparison of different synergistic PET-MR image reconstruction of the in-vivo PET-MR dataset.

257x170mm (300 x 300 DPI)